


# **National Chiao Tung University**

Department of Applied Chemistry

PhD Thesis

**Structure and Dynamics of Transient Species  
Produced in Condensed-Phase Photophysical and  
Photochemical Reactions as Elucidated by  
Nanosecond Time-Resolved Near/Mid-IR  
Spectroscopy**

The logo of National Chiao Tung University is a circular seal. It features a central emblem with a book and a lamp, surrounded by the university's name in Chinese and English. The year '1896' is inscribed at the bottom of the seal.

Student: Sudhakar Narra

Advisor: Dr. Shinsuke Shigeto

September 2014

**Structure and Dynamics of Transient Species  
Produced in Condensed-Phase Photophysical and  
Photochemical Reactions as Elucidated by  
Nanosecond Time-Resolved Near/Mid-IR  
Spectroscopy**

Student: Sudhakar Narra

Advisor: Dr. Shinsuke Shigeto



Submitted to Ph. D. Program, Department of Applied Chemistry  
College of Science

National Chiao Tung University  
in Partial Fulfillment of the Requirements  
for the Degree of Doctor of philosophy  
in  
Applied Chemistry

September 2014

Hsinchu, Taiwan, Republic of China

# Structure and Dynamics of Transient Species Produced in Condensed-Phase Photophysical and Photochemical Reactions as Elucidated by Nanosecond Time-Resolved Near/Mid-IR Spectroscopy

Student: Sudhakar Narra

Advisor: Dr. Shinsuke Shigeto

Ph. D. Program, Department of Applied Chemistry

National Chiao Tung University



In this Thesis, the author presents unprecedentedly detailed studies on the structure and dynamics of ionic and neutral transient species that are of crucial importance in molecular photovoltaic devices, using nanosecond time-resolved near/mid-IR spectroscopy with the help of density functional theory (DFT) calculations and chemometrics techniques. The author has investigated (1) the back electron transfer (BET) dynamics in photoinduced intermolecular electron transfer reaction between pyrene (Py) and 1,4-dicyanobenzene (DCB) in acetonitrile and (2) the structure of the lowest excited triplet ( $T_1$ ) state of *p*-nitroaniline (PNA) in acetonitrile- $d_3$ . In the first work, the transient near/mid-IR spectra of Py radical dimer cation and DCB radical anion are observed in the nano- to microsecond (ns– $\mu$ s) time regime after photoexcitation of Py. Global fitting analysis of the time-resolved IR data reveals a dual role of acetonitrile as solvent and “charge mediator” of the charge recombination between Py radical dimer cation and DCB radical anion in the BET reaction. This finding may have implications for dye-sensitized solar cells because acetonitrile is a commonly used solvent for redox couples in these types of devices. In the second work, the transient mid-IR spectra of

PNA in the  $T_1$  state generated after photoexcitation of PNA and subsequent intersystem crossing are examined to characterize the structure of  $T_1$  PNA. Comparison of the experimental IR spectra with DFT calculated results on explicitly solvated PNA shows that  $T_1$  PNA has a partial quinoid structure, which sharply contrasts with the well-known zwitterionic charge-transfer structure of the lowest excited singlet state of PNA. The studies presented in this Thesis not only illustrate the applicability of the time-resolved near/mid-IR method to a wide variety of important photophysical and photochemical processes in the condensed phase, but they also provide otherwise hardly obtainable insights into the structure and dynamics of transient species (radicals and excited-state molecules) involved in charger transfer processes.



## Acknowledgements

I would like to express my sincere gratitude to my supervisor Prof. Shinsuke Shigeto for accepting me as his doctoral student, mentoring me and making this thesis possible. I am thankful for his counsel and critical insights that has led me to advance both professionally and personally during my doctoral studies at ultimate spectroscopy and imaging laboratory (USIL). I am equally thankful to Prof. Hiro-o Hamaguchi for spending his valuable time to discuss my research results. He served as an inspiration to me during this study and I enjoyed both scientific and non-scientific discussions with him during teatime. I will always be grateful to Prof. Satyen Saha for helping me to join at USIL as a graduate student, encouraging me during his visits to USIL, taking good care of me and offering his insights.

I am deeply indebted to my collaborators Prof. Henryk Witek, Dr. Yoshifumi Nishimura and Mr. Shu Wei-Chang for their help with the theoretical calculations. Their calculation results helped me to assign the vibrational bands of the transients and explain the bonding structure of p-Nitroaniline in a detailed manner.

My heartfelt thanks goes to my senior Dr. Sohshi Yabumoto for teaching me how to perform experiments, align nanosecond time-resolved IR spectrometer and spending an adequate amount of time with me to discuss about my experiments and give his critical inputs to improve them to a great deal. I am fortunate to have a senior like him.

I am thankful to Dr. Rintaro Shimada and Dr. Hajime Okajima for showing an immense interest in my research and discussing with me, debating with me at times and giving their valuable suggestions. Textbook reading sessions with Dr. Shimada were always stimulating and I could broaden my understanding on various fundamental concepts of optics and spectroscopy. Low-frequency Raman experiments with Dr. Okajima were always enjoyable.

I thank my friend Mr. Murali Krishna Pola for assisting me with the synthesis of p-Nitroaniline isotopomers and recording  $^1\text{H-NMR}$  spectra for those synthesized compounds.

Special thanks to my friend Mrs. Zahra Hosseini for showing interest in my work on BET reaction mechanisms and expressing her inputs on electron transfer phenomenon in photovoltaics.

It is always good to have your close friend as a colleague. I am blessed to have one in the form of Dr. Hemanth Nag Noothalapati Venkata. I am thankful to him in every possible way for being a good support system during this study.

I would also like to thank Dr. Chuang-Keng Huang, Dr. Vitaly Korepanov and Dr. Ashok Z. Samuel for their encouragement.

I am thankful to all the present and past members of USIL for their support throughout my doctoral studies whenever needed.

I thank my close friends and parents for the care, love and emotional support they have extended during my study without which the present thesis is not possible.

Finally, I would like to thank “Scholarship Program of Taiwan” aka. Taiwan Scholarship and Prof. Shigeto for their financial assistance.

–Sudhakar

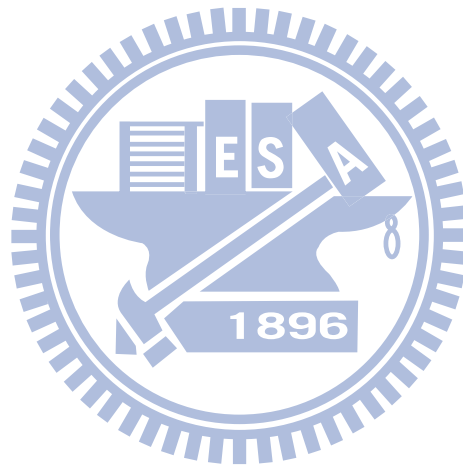


# Table of Contents

Abstract.....	i
Acknowledgements.....	iii
Table of Contents .....	v
List of Figures .....	vi
List of Tables.....	ix
List of Schemes .....	ix
Chapter I Introduction .....	1
Chapter II Nanosecond Time-resolved Near/Mid-IR spectrometer and Data Analysis	
Techniques .....	5
<b>II-1 Introduction</b> .....	6
<b>II-2 Nanosecond Time-resolved Dispersive IR Spectrometer</b> .....	6
II-2.1 TRIR Setup .....	7
II-2.2 Sample Circulation System.....	10
<b>II-3 Singular Value Decomposition Analysis</b> .....	11
II-3.1 Mathematical Definition.....	11
<b>II-4 Global Fitting Analysis</b> .....	12
Chapter III BET Mechanism of a Bimolecular PET Reaction between Py and DCB.....	15
<b>III-1 Introduction</b> .....	16
<b>III-2 Materials and Methods</b> .....	18
III-2.1 Materials .....	18
III-2.2 Nanosecond Time-resolved Near/Mid-IR Spectroscopy.....	18
III-2.3 Computational Details .....	19
<b>III-3 Results and Discussion</b> .....	19
III-3.1 Nanosecond TRNIR/MIR Spectra of Py and DCB in ACN Solution Measured under Ar Bubbling.....	19
III-3.2 Vibrational Assignments .....	20
III-3.3 Molecular Oxygen Quenching Experiment.....	22
III-3.4 Kinetic Analysis .....	23

III-3.5 Concentration Dependence Studies of the BET Reaction between Py and DCB in ACN Solution.....	27
III-3.6 TRIR Spectra of Py and DCB in Benzene Solution .....	28
<b>III-4 Summary.....</b>	<b>29</b>
<b>Chapter IV Structural Elucidation on the T<sub>1</sub> State of PNA in CD<sub>3</sub>CN Solution .....</b>	<b>30</b>
<b>IV-1 Introduction .....</b>	<b>31</b>
<b>IV-2 Materials and Methods .....</b>	<b>32</b>
IV-2.1 Sample Preparation Methods .....	32
IV-2.2 Nanosecond Time-Resolved Infrared Spectroscopy.....	33
IV-2.3 Computational Details .....	34
<b>IV-3 Results and Discussion .....</b>	<b>34</b>
IV-3.1 Nanosecond TRIR Spectra of PNA in CD <sub>3</sub> CN under Ar Environment .....	34
IV-3.2 SVD analysis of the TRIR Spectra of PNA in CD <sub>3</sub> CN .....	36
IV-3.3 TRIR Spectra of PNA in CD <sub>3</sub> CN under O <sub>2</sub> Environment .....	37
IV-3.4 Experimental IR Spectra of the T <sub>1</sub> State of PNA and Its Isotopomers .....	39
IV-3.5 Calculated IR spectra of the T <sub>1</sub> State of PNA and Its Isotopomers .....	42
<b>IV-4 Structural of T<sub>1</sub> PNA.....</b>	<b>46</b>
<b>IV-5 Summary.....</b>	<b>48</b>
<b>Chapter V Conclusions and Future Prospects .....</b>	<b>49</b>
<b>References .....</b>	<b>51</b>

### List of Figures

Figure II–1. Optical layout of the nanosecond TRIR spectrometer. ....	9
Figure II–2. Schematic of the cell holder. ....	10
Figure II–3. Schematic of the sample circulation system. ....	11
Figure II–4. Simulated time-resolved spectra (a), extracted concentration profiles (b), spectral profiles (c) and residuals (d) obtained after performing global curve fitting analysis over the time-resolved spectral data matrix shown in (a). ....	14
Figure III–1. UV/Vis spectra of Py (red solid curve) and DCB (black solid curve) in ACN solution. Also shown is the UV/Vis spectrum of the ACN solution of both Py and DCB (grey dashed curve). In all solutions, the concentrations of Py and DCB were 0.50 and 5.0 mM, respectively. The molar extinction coefficient of Py at the excitation wavelength (355 nm) is 280 M <sup>-1</sup> cm <sup>-1</sup> , whereas that of DCB is one order of magnitude smaller. ....	17



Figure III–2. Left: Time-resolved IR spectra in the regions 3800–12000 $\text{cm}^{-1}$ (a), 2000–2200 $\text{cm}^{-1}$ (b), and 1120–1260 $\text{cm}^{-1}$ (c), of Py and DCB dissolved in ACN (0.50 and 5.0 mM, respectively) excited at 355 nm with Ar bubbling. The spectra in (a) are masked at around 4400 $\text{cm}^{-1}$ due to an overtone band of the solvent. Each time-resolved spectrum is offset by $4 \times 10^{-5}$ for clarity of display. Right: Time profiles at 11000 (d), 6800 (e), 2100 (f), 1216 (g), and 1136 (h) $\text{cm}^{-1}$ . The smooth black curves are the result of the kinetic analysis based on the reaction mechanism shown in Scheme III–1.....	20
Figure III–3. (a) FTIR spectrum of Py (30 mM) in $\text{CD}_3\text{CN}$ . (b) DFT/B3LYP calculated IR spectrum of the gas phase Py molecule (plotted using a Gaussian band envelop with a FWHM of 10 $\text{cm}^{-1}$ ). (c) Transient IR spectrum at 0–5 $\mu\text{s}$ , same as the top trace of Figure III-1c. (d) DFT/B3LYP calculated IR spectrum of gas phase $\text{Py}_2^{*+}$ .....	21
Figure III–4. Time-resolved near- and mid-IR spectra of Py (0.50 mM) and DCB (5.0 mM) dissolved in ACN, measured at 0–5 $\mu\text{s}$ with Ar (top) and $\text{O}_2$ (bottom) bubbling. The spectrum taken with Ar bubbling is offset by $4 \times 10^{-5}$ for clarity of display.....	22
Figure III–5. Two-dimensional (2D) plots of the observed time-resolved spectra (a), the fitted result (b), and the residue (c). Each of the three 2D plots is represented in a rainbow pseudo color scale: the highest $\Delta A$ value appears red and the lowest appears purple. Note that the maximum $\Delta A$ value is $5 \times 10^{-5}$ in (a) and (b) and $5 \times 10^{-6}$ in (c).....	26
Figure III–6 Left: Time-resolved IR spectra in the regions 3800–12000 $\text{cm}^{-1}$ (a), 2000–2200 $\text{cm}^{-1}$ (b), and 1120–1260 $\text{cm}^{-1}$ (c), of Py and DCB dissolved in ACN (5.0 and 5.0 mM, respectively) excited at 355 nm with Ar bubbling. Each time-resolved spectrum is offset by $2 \times 10^{-4}$ for clarity of display. Right: Time profiles at 11000 (d), 6800 (e), 2100 (f), 1216 (g), and 1136 (h) $\text{cm}^{-1}$ . The smooth black curves are the result of the kinetic analysis based on the reaction mechanism shown in Scheme III–1.....	27
Figure III–7. Left: Time-resolved near- and mid-IR spectra of Py (5.0 mM) and DCB (50 mM) dissolved in benzene, excited at 355 nm with argon bubbling. Each spectrum is offset by $1 \times 10^{-4}$ for clarity of display. Asterisks indicate an interference from a solvent band in the mid-IR region and a bleach due to the stimulated emission of Py in the near-IR region. Right: Averaged time profiles of the transient bands between 10400–3900, 1232–1188 and 2144–2040 $\text{cm}^{-1}$ (dots). The smooth curves are fits to an exponential function convolved with a Gaussian instrumental response function.....	29
Figure IV–1. Representative resonance structures of PNA and their hybrids: neutral form (1), zwitterionic form (2), and partial quinoid form (3).....	31

Figure IV–2. UV-Vis Spectrum of PNA (500 $\mu\text{M}$ ) in $\text{CD}_3\text{CN}$ . Brown line represents the laser excitation wavelength (355 nm) chosen for pumping PNA to the $S_1$ state. ....	33
Figure IV–3. Ground-state ( $S_0$ ) spectrum (a) and time-resolved IR difference spectra (b) of PNA in $\text{CD}_3\text{CN}$ (0.25 mM), excited at 355 nm with Ar bubbling. Each time-resolved spectrum is offset by $5 \times 10^{-5}$ for clarity. ....	35
Figure IV–4. (a) Plot of singular values obtained from the SVD of the TRIR data matrix. (b,c) Spectral (b) and temporal (c) components corresponding to the largest three singular values. Each spectral and temporal component is offset by 0.3 and 0.2 respectively, for clarity. ....	36
Figure IV–5. Results of a SVD analysis of the time-resolved IR difference spectra of PNA in $\text{CD}_3\text{CN}$ with Ar bubbling. (a) Decomposed spectral component. (b) Decomposed temporal component (red line) and the best fit (black line) to an exponential function convolved with a Gaussian IRF. The exponential time constant is determined to be $\tau = 430$ ns. ....	37
Figure IV–6. (a) Time-resolved IR difference spectra of PNA in $\text{CD}_3\text{CN}$ with $\text{O}_2$ bubbling: 0–200 ns and 200–400 ns after photoexcitation. (b) Kinetic profiles of the transient band at $1248 \text{ cm}^{-1}$ with Ar bubbling (red circle) and with $\text{O}_2$ bubbling (blue triangle). The time profiles have been normalized to the same maximum height. Solid lines are the best fits to an exponential convolved with a Gaussian IRF. ....	38
Figure IV–7. Upper panels: experimental IR spectra of PNA (red line) and its isotopomers, PNA- $^{15}\text{NH}_2$ (blue) and PNA- $^{15}\text{NO}_2$ (green). (a–c) Ground-state ( $S_0$ ) spectra recorded with an FT-IR spectrometer. (d–f) Lowest excited triplet-state ( $T_1$ ) spectra obtained by compensating the depletion of the ground-state absorption. Lower panels: calculated IR spectra of PNA (red line), PNA- $^{15}\text{NH}_2$ (blue), and PNA- $^{15}\text{NO}_2$ (green), using the PNA+2ACN model with (solid line) and without (dotted line) elongation of the C– $\text{NH}_2$ bond by $0.012 \text{ \AA}$ . (g–i) The ground state. (j–l) The $T_1$ state. See text for details. ....	40
Figure IV–8. Comparison of experimental and theoretical DFT/B3LYP IR spectra of PNA in the ground state. (a) FT-IR spectrum of PNA in $\text{CD}_3\text{CN}$ (0.25 mM), (b) a gas-phase molecular model, (c) the PCM model, (d) an explicitly solvated model with two $\text{CD}_3\text{CN}$ molecules attached to the $\text{NH}_2$ group (the PNA+2ACN model), (e) the PNA+2ACN model with elongation of the C– $\text{NH}_2$ bond by $0.012 \text{ \AA}$ , and (f) an explicitly solvated model with six $\text{CD}_3\text{CN}$ molecules. ....	43
Figure IV–9. Optimized geometries of the PNA+2ACN (a) and PNA+6ACN (b) models. ....	44
Figure IV–10. Bond lengths and bond angles in the $S_0$ state (upper value) and $T_1$ state (lower value in green) derived from the DFT calculations with the PNA+2ACN model. ....	48

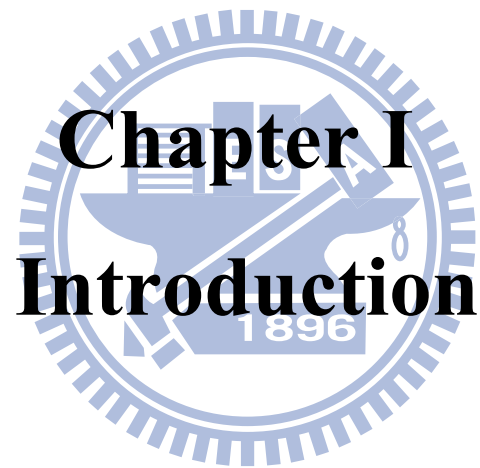
## List of Tables

Table IV–1. Experimental and Calculated Vibrational Frequencies and Assignments of Major IR Bands (in 1200–1700 $\text{cm}^{-1}$ ) of PNA, PNA- $^{15}\text{NH}_2$ , and PNA- $^{15}\text{NO}_2$ in the Ground State and the Lowest Excited Triplet State. ....	41
---	----

## List of Schemes

Scheme III–1. Top: $\text{DCB}^{\bullet-}$ ejects an electron into the solvent ACN, resulting in the formation of neutral DCB and $\text{ACN}_2^-$ . Bottom: $\text{Py}_2^{\bullet+}$ captures the excess electron in $\text{ACN}_2^-$ . ....	24
---	----





Many of the fascinating events of this universe happen in the blink of an eye. Human evolution thrives on deciphering the mysteries of these events. Among these fascinating events, light–matter interactions have allured many researchers due to their significant implications in various processes that occur in our nature and this led to the development of a field of science called photochemistry [1]. Photosynthesis [2,3], vision [4,5], C—C bond cleavage [6,7] and photochromism [8,9] are classic examples of photochemical processes that can be seen in our nature. The trigger for these photochemical reactions is often the structural changes associated with the absorption of light by the molecule. Unraveling the mechanisms of these light-driven events enables us to mimic the sophisticated strategies found in the nature, which will eventually turn out to be the shortest way to the development of sustainable and cleaner energy sources.

To elucidate underlying mechanisms of photochemical processes, it is essential to study the dynamics and molecular structure of the transient species (e.g., excited states, radicals and ions) that are responsible for the reactivity of the reactants [10]. For example, Norrish type II reactions are very inefficient in aromatic esters if the lowest excited singlet ( $S_1$ ) state of the molecule has a  $\pi$ – $\pi^*$  character. However, these reactions proceed efficiently if the  $S_1$  state is of charge transfer (CT) character [11]. Similarly, in the case of acetophenones, the lowest electronic triplet ( $T_1$  and  $T_2$ ) states are closely lying and are in thermal equilibrium with each other [12]. In such a situation, the nature of the  $T_1$  state alone cannot account for the reactivity of the molecule towards photoinduced H-atom abstraction. Thus, detailed information about the electronic excited states using spectroscopic approaches is required and allows material chemists to design new chromophores for applications in organic light emitting diodes (OLEDs), organic photovoltaics (OPVs), photocatalysts, etc. As these electronic excited states or transient species are short-lived, time-resolved spectroscopy [13,14] is undoubtedly the best choice to study their molecular structures and dynamics.

Photochemical reactions usually occur over a broad timescale ranging from few tens of femtoseconds to few thousands of seconds. The fastest reactions are seen in wave packet motion of molecular vibrations and photoinduced electron transfer (PET) (ionization), whereas the slowest reactions are observed as phosphorescence of molecules. Time-resolved spectroscopy had started after the advent of flash photolysis established by Porter [15,16], progressed concurrently with the developments in ultrafast laser technology, and already reached the femtosecond time regime [17,18]. One can now obtain the information of excited states ranging from few femtoseconds up to few hundreds of microseconds using pulsed lasers with different pulse durations. Researchers have used both transient absorption [19,20]

and time-resolved vibrational (IR [21-24] and Raman [25-28]) spectroscopies to elucidate the structural and dynamic information of excited states. Nevertheless, more thorough understanding of excited states is far from completion. Here in this Thesis, we present results of two fundamentally important experiments in which we try to advance our understanding of the reaction dynamics and nature of excited states in the condensed phase.

In the present study, nanosecond time-resolved IR (TRIR) spectroscopy is used to reveal the structure and dynamics of transients associated with the photophysical and photochemical pathways of PET reactions. Vibrational spectroscopy is inherently sensitive to the molecular structure of transient species. For instance, the frequency of a specific vibrational mode of the transient may reflect changes in bond length between the excited state and the ground ( $S_0$ ) state [23,29], which in turn provides information about changes in the structure of the molecule. Transient absorption spectroscopy in the visible region is also capable of producing such shifts in electronic bands relative to the  $S_0$  spectrum. However, it is not possible to know using transient absorption spectroscopy which part of the molecule is prone to change and to what extent compared with the other part. Such structural information can be more directly obtained from vibrational spectra. Moreover, electronic absorption bands are very broad and they may overlap with each other when the reaction of interest involves more than one transient species as in the case of benzophenone, of which  $T_1$  state and ketyl radical absorptions fall in the same spectral region [30]. In contrast, IR bands are normally narrower and specific to particular functional groups of the molecule. These characteristics make TRIR spectroscopy ideal for the study of molecular structure and dynamics of transients involved in PET reactions.

Broadly, PET reactions are classified into two types [31]: intermolecular and intramolecular PET reactions. If an electron is transferred from excited-state donor to ground-state acceptor or from a ground-state donor to excited-state acceptor, such a reaction is termed an intermolecular PET reaction. Intramolecular PET reactions is a class of reactions where an electron is transferred between donor and acceptor moieties within the same molecule in its electronic excited state. Both of the reactions are fundamentally important owing to their significance in the OPV applications. For example, the functioning of solar cells is purely based on consecutive ET processes. Both charge creation and charge annihilation are crucial for the performance of these photovoltaic devices. Charge recombination and relaxation of dye molecules to the triplet manifold are considered as a loss mechanism in organic solar cells. In other words, it is desirable for the excited molecule to remain in the charge-separated state for a long time. The back electron transfer (BET) reaction in an intermolecular electron

transfer reaction is the mirroring of the reaction of regeneration of dye molecules in dye-sensitized solar cells (DSSCs). Similarly, in solid-state solar cells where compact donor acceptor (D–A) dyads are used, excitation losses via relaxation to a triplet state are significant. It is therefore quite important to understand the nature of the triplet state of such chromophores. In this Thesis, we try to shed light on a BET reaction and triplet structure using TRIR.

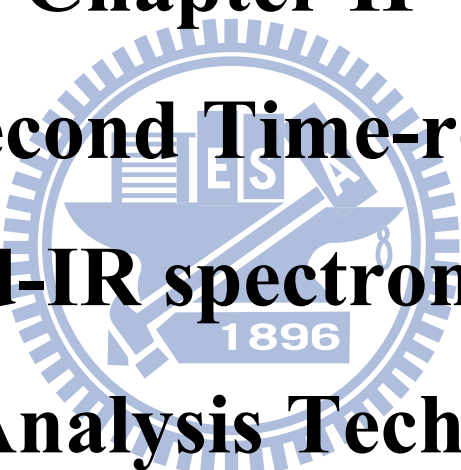
The rest of this Thesis consists of four chapters. Chapter II deals with the experimental and data analysis techniques we used to perform experiments and interpret the results. This involves the technical details of the laboratory-built nanosecond TRIR spectrometer that is capable of measuring the near/mid-IR spectrum between 800–12000  $\text{cm}^{-1}$  and a laboratory-built sample circulation system. It is worthy to mention that the present experiments have been made possible owing to high sensitivity of the spectrometer, i.e., absorbance changes as low as  $1 \times 10^{-6}$ . Theoretical principles of singular value decomposition (SVD) analysis and global curve fitting techniques are also explained very briefly.

In Chapter III, the BET reaction mechanism between pyrene (Py) and 1,4-dicyanobenzene (DCB) in acetonitrile (ACN) solution is studied using the spectra recorded in both near- and mid-IR (NIR and MIR) regions. Here Py and DCB serve as a model system in which forward electron transfer (FET) is accomplished rapidly because of symmetry matching between the LUMO of Py and LUMO of DCB, whereas BET is retarded because of symmetry mismatch between the LUMO of DCB and HOMO of Py. It is interesting to reveal what would govern the BET reaction where a direct recombination of the generated ion pair is restricted by orbital symmetry, which is usually the case in organic solar cells. A reaction mechanism is proposed that can explain the observed kinetics of NIR and MIR transients (radical cation and anion in the present case).

In Chapter IV, the bonding structure of the  $T_1$  state of *p*-nitroaniline (PNA) is studied in acetonitrile- $d_3$  ( $\text{CD}_3\text{CN}$ ) solution using MIR spectra between 1200–1700  $\text{cm}^{-1}$ . PNA serves as a model compound for push-pull chromophores or D–A type dyads. PNA exhibits a CT state in the  $S_1$  state. A similar CT structure would be expected for the  $T_1$  state as well, but this remains to be tested experimentally. A unique structure of  $T_1$  PNA is proposed on the basis of experimental results of PNA and its isotopomers as well as DFT calculations using an explicit solvation model.

Finally, conclusions and future prospects are given in Chapter V.

**Chapter II**  
**Nanosecond Time-resolved**  
**Near/Mid-IR spectrometer and**  
**Data Analysis Techniques**





## II-1 Introduction

In this chapter, we present technical details of the laboratory-built nanosecond TRIR spectrometer used in this work and the principles of numerical data analysis techniques (SVD and global curve fitting) employed for physical interpretation of observed spectroscopic results.

## II-2 Nanosecond Time-resolved Dispersive IR Spectrometer

Nanosecond TRIR spectroscopy is a well-known technique used to study the photophysical and photochemical processes that are taking place in the sub microsecond to millisecond time domains. The development of nanosecond dispersive TRIR spectrometers dates back to 1990s. Yuzawa and co-workers [32] developed a high-sensitivity nanosecond TRIR spectrometer by using a high-intensity IR light source and an ultralow-noise, wide-bandwidth amplifier. However, long acquisition time and poor spectral resolution were the major drawbacks of their apparatus. Yabumoto and co-workers [12,33] improved the spectral resolution of the apparatus by enhancing the throughput of the spectrometer. More specifically, they employed a long-focal-length spectrometer with a low f-number. It was further modified to cover a wider spectral range of both NIR and MIR regions so that one can access not only vibrational transitions but also low-energy electronic transitions that are dark to visible spectroscopy. In the present study, we used the TRIR spectrometer originally developed by Dr. Sohshi Yabumoto [33].

Time-resolved Raman spectroscopy is a complementary approach to TRIR spectroscopy [27,28,34,35]. Although both techniques provide essentially the same vibrational information except that different selection rules apply to Raman and IR, TRIR spectroscopy has a couple of advantages over time-resolved Raman spectroscopy in studying the reaction mechanisms of photochemical reactions. First, fluorescence, which often accompanies photophysical and photochemical reactions, severely interferes with Raman measurements. Second, time-resolved Raman spectroscopy requires the probe light to be in resonance with an electronic transition from the excited state generated by the pump pulse. This requirement implies that at the expense of high selectivity due to the resonance Raman effect, only the information of the excited states that can be resonantly excited will be obtained with time-resolved Raman spectroscopy. If we are interested in seeing the whole reaction dynamics rather than particular transient species that is in resonance with the probe light, we should choose a technique that does not utilize resonance enhancement, i.e., TRIR.

## II-2.1 TRIR Setup

The TRIR spectrometer used in the present study is schematically shown in Figure II–1. It consists of a photoexcitation light source, an IR probe light source, a dispersive monochromator, a slit controller, a high-speed detector, a differential amplifier, and a high-speed digitizer. The photoexcitation light source was a Q-switched Nd-YAG laser (IB Laser, DiNY pQ 355), which emits the third harmonic at 355 nm. The pulse width was 7 ns and repetition rate was 500 Hz. The maximum pulse energy was 1.1 mJ, but typically pulse energy of ~100–150  $\mu\text{J}$  was used for photoexcitation. A ceramic IR emitter purchased from JASCO was used as the probe light for MIR measurements ( $<4000\text{ cm}^{-1}$ ), whereas a tungsten-halogen lamp was used for NIR measurements ( $>4000\text{ cm}^{-1}$ ). The probe IR light was focused onto the sample and was introduced into a modified Czerny–Turner monochromator (JASCO, CT-50TFP; focal length = 500 mm and F-number = 4.3) using a pair of off-axis ellipsoid mirrors. The probe light transmitted through the sample was dispersed by the monochromator. The dispersive method utilized in the present study excels the FTIR method in sensitivity [12], [36], stability, and less influence of artifacts [32]. Three manually switchable gratings are available in this monochromator. The groove density and blaze wavelengths of these gratings are as follows: (i) 100 lines  $\text{mm}^{-1}$  and 7.3  $\mu\text{m}$ ; (ii) 300 lines  $\text{mm}^{-1}$  and 3  $\mu\text{m}$ ; and (iii) 600 lines  $\text{mm}^{-1}$  and 10  $\mu\text{m}$ . These three gratings can cover the spectral window between 800 and 11500  $\text{cm}^{-1}$ . Higher-order diffraction was removed by using an order sorter after the exit slit of the monochromator that comprises appropriate filters attached to a filter wheel. When the tungsten-halogen lamp was used, the visible portion of the output was eliminated by using a pair of IR transmitting filters (Sigma Koki, ITF 85IR): one before the sample and the other in front of the entrance slit of the monochromator. The entrance and exit slits of the monochromator were controlled precisely by an external OPTMIKE slit controller to keep the spectral resolution constant throughout the measurement. The mechanical slit width ( $S_m$ ) at any given spectral resolution identical to its optical slit width ( $S_{sp}$ ) for a Czerny–Turner type monochromator is given by Eq. (II–1).

$$\begin{aligned}
 S_m &= \frac{S_{sp}}{d_{\tilde{\nu}}} \\
 &= \frac{10S_{sp} \text{ mfG}}{\tilde{\nu}_0^2 \cos \left\{ \varepsilon + \arcsin \left( \frac{5mG}{\tilde{\nu}_0 \cos \varepsilon} \right) \right\}}
 \end{aligned}
 \tag{II-1}$$

Here  $d_{\tilde{\nu}}$  is the linear dispersion in wavenumber,  $m$  is the order of diffraction,  $f$  is the focal length,  $G$  is the groove density of the grating used,  $\tilde{\nu}_0$  is the center wavenumber, and  $\varepsilon$  is the half value of the Ebert angle, which is the angle between the incident and diffracted lights at the grating. The Ebert angle of the CT-50 monochromator is  $27^\circ$ .

The dispersed light was further focused on the IR light detector using an off-axis ellipsoid condenser. A mercury cadmium telluride (MCT) detector was used for the region below  $2000 \text{ cm}^{-1}$  and an indium antimonide (InSb) detector for the region above  $2000 \text{ cm}^{-1}$ . The bandwidths of the MCT and InSb detectors were 20 and 15 MHz, respectively. The detected signal from the IR detector was amplified by coupling the detector output with an ultralow-noise preamplifier using a 22 nF capacitor, followed by further amplification by a factor of 1000 with a differential amplifier (NF Corporation, 5305; 10–1000 amp. gain, 10 MHz bandwidth) so that only the small changes in the probe light intensity induced by the pump pulse can be detected. Owing to this AC-coupled amplification, the sensitivity of the instrument reaches as high as  $1 \times 10^{-6}$ . The time resolution of the instrument is limited by the bandwidth of the differential amplifier, which is approximately 80 ns.

The output of the main amplifier was fed to a high-speed digitizer (NI, 5112; dynamic range = 8 bit, sampling rate = 100 MHz) mounted on a personal computer. The apparatus is also equipped with another digitizer from Tektronix (DSA 602A), which was used for measurements with a sampling rate higher than 100 MHz. However, the data transfer throughput between the oscilloscope and the computer is low because of GPIB communication.

The procedures for measuring steady-state and time-resolved difference IR spectra are as follows. The intensity of the IR probe light,  $I(\tilde{\nu}_0)$ , and the intensity of the IR probe light transmitted through the sample,  $I(\tilde{\nu})$ , were measured consecutively. The probe light was modulated by a rectangular wave generated by a chopper in order to measure the intensity in the AC-coupled amplification detection scheme. The absorbance of the sample is calculated using Beer–Lambert law.

$$A(\nu) = -\log\left(\frac{I(\tilde{\nu})}{I(\tilde{\nu}_0)}\right) \quad (\text{II-2})$$

The IR absorbance difference ( $\Delta A$ ) spectrum was measured by spatially overlapping the pump pulse and probe light at the sample. The beam diameter of the probe light was about 2 mm at the sample position. The 355-nm pump beam was loosely focused so that it can illuminate a sufficiently large area of the probe beam. The small changes in the intensity of the probe light

induced by photoexcitation with the pump pulse was measured using the AC-coupled detection scheme. The measured  $\Delta A$  spectrum is substantially interfered with Q-switch noise, thermal noise of the detector, and other electronic noises. To achieve a high signal-to-noise ratio (S/N), it is desirable to reduce all these noises as much as possible. To eliminate Q-switch noise, the IR detector was shielded using a box made of aluminium. Cross talk between the cables was reduced by optimizing cable orientations and appropriately grounding the electronic devices. The intensities of the probe beam with pump on and off were measured in sequence and the pump-off spectrum was subtracted from the pump-on spectrum to obtain the time-dependent change in the intensity of the probe light,  $\Delta I(\tilde{\nu}, \tau)$ . The time-dependent absorbance change  $\Delta A$  is given by Eq. (II-3).

$$\Delta A(\tilde{\nu}, \tau) = -\log \left( 1 + \frac{\Delta I(\tilde{\nu}, \tau)}{I(\tilde{\nu})} \right) \quad (\text{II-3})$$

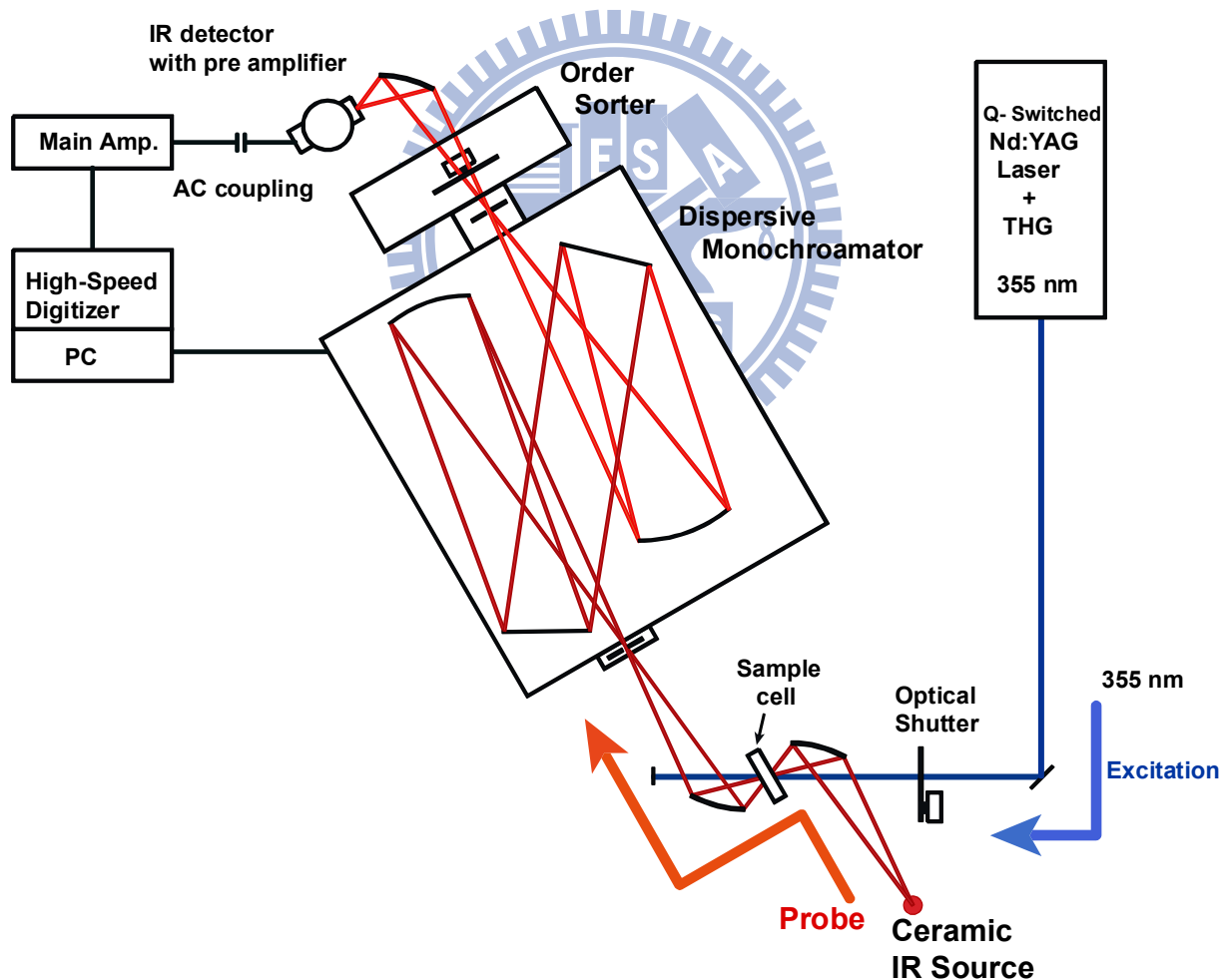


**Figure II-1.** Optical layout of the nanosecond TRIR spectrometer.

## II-2.2 Sample Circulation System

TRIR measurements were performed using a sample circulation system that allows us to have a fresh sample for every new pulse at the sample. This sample circulation system prevents the sample from degradation due to multiple excitation with the pump pulses. It consists of a sample cell holder, IR-transparent optical windows, Karlez® O-rings, Teflon® tubing, Swagelok® bulkhead unions, a gear pump driven by magnetic field (IDEX Co.), and a reservoir. Schematics of the sample cell holder components and the entire sample circulation system are shown in Figure II–2 and Figure II–3, respectively. The sample cell holder is made of stainless steel and has very flat and smooth surface with holes to accommodate the O-rings. The inlet and outlet of the sample holder were connected to the gear pump and sample reservoir, respectively, using Teflon tubing to enable sample circulation. Optical-grade calcium fluoride and barium fluoride plates (thickness = 20 mm), which are transparent throughout the visible and IR regions, were used as optical windows. A lead spacer was sandwiched by these optical windows. Depending on the sample and the spectral region to be measured, the path length of the cell was varied by changing the thickness of the spacer. Typically 50, 100, and 500  $\mu\text{m}$  spacers were used for MIR measurements, whereas a 1 mm spacer was used for NIR measurements because of very weak signal intensity in this region.

The sample was circulated using the gear pump at a flow rate of 20 cm/s. The sample in the reservoir was bubbled with argon gas to remove dissolved molecular oxygen ( $\text{O}_2$ ).

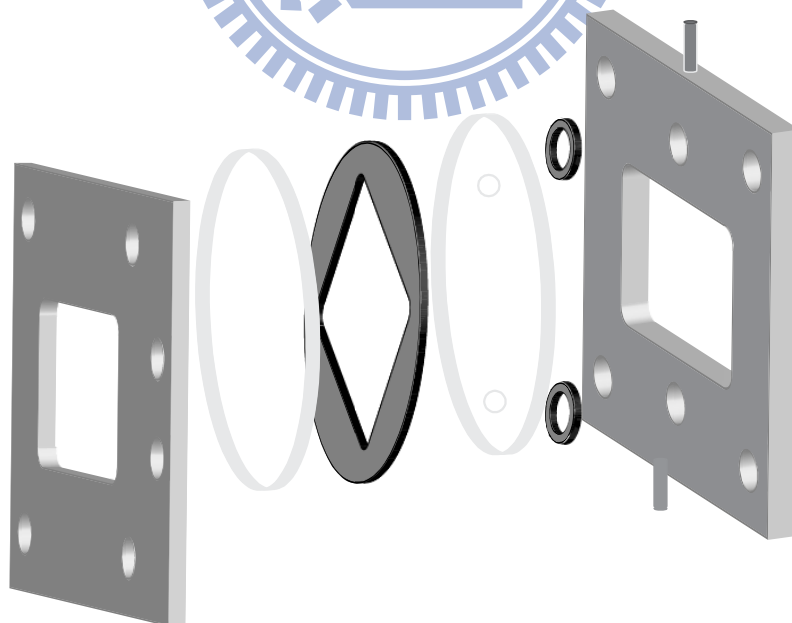


**Figure II–2.** Schematic of the cell holder.

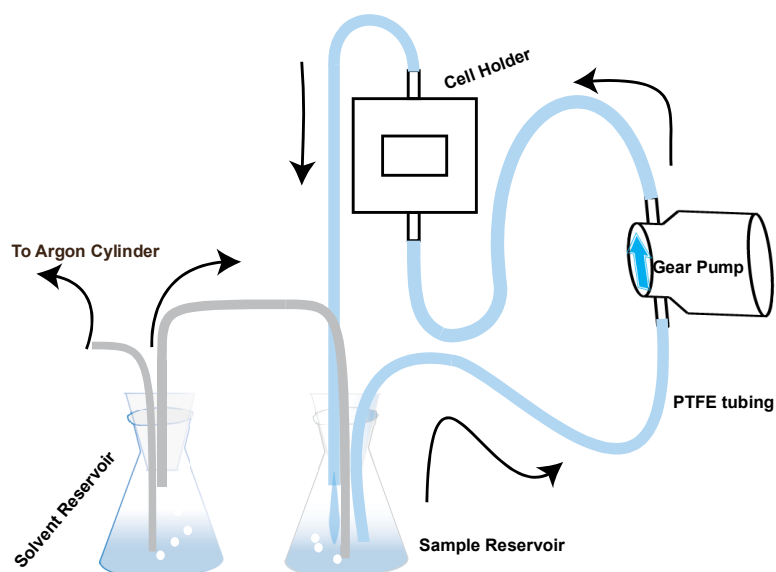


**Figure II–3.** Schematic of the sample circulation system.

## II-3 Singular Value Decomposition Analysis

SVD analysis is one of the most popular multivariate data analysis techniques used by spectroscopists to extract the information on the number of significant components involved in the spectra measured as a function of time, temperature, pH, concentration, etc. SVD analysis has previously been used in TRIR spectroscopy [37-39] to interpret the transient spectra based on a physical model. If the data reconstructed using the model reproduce the original data well within experimental uncertainty, we can conclude that the model represents a plausible mechanism of the underlying photophysical or photochemical processes. SVD was employed in the PNA work (see Chapter IV).

### II-3.1 Mathematical Definition

Given a real  $m \times n$  matrix  $\mathbf{A}$ , SVD decomposes it as

$$\mathbf{A} = \mathbf{U}\mathbf{S}\mathbf{V}^T \quad (\text{II-4})$$

where  $\mathbf{U}$  is an  $m \times m$  orthogonal matrix,  $\mathbf{V}$  is an  $n \times n$  orthogonal matrix, and  $\mathbf{S}$  is an  $n \times n$  diagonal matrix. The columns of  $\mathbf{U}$  are the left singular vectors of  $\mathbf{A}\mathbf{A}^T$  and the rows of  $\mathbf{V}^T$  are the right singular vectors of  $\mathbf{A}^T\mathbf{A}$ . The diagonal matrix  $\mathbf{S}$  is called a singular value matrix and its diagonal elements are called singular values, which are nothing but the square roots of the eigenvalues of either of the left singular vectors  $\mathbf{u}_k$  or the right singular vectors  $\mathbf{v}_k$ . These

singular values are placed in a decreasing order ( $s_{11} > s_{22} > s_{33} > \dots > s_{rr} > \dots > s_{nn}$ ) along the diagonal of the matrix  $\mathbf{S}$ . The matrix notation of SVD is shown in Eq. (II-5).

$$\begin{bmatrix} a_{11} & \cdots & a_{1n} \\ \vdots & \ddots & \vdots \\ \vdots & \cdots & \vdots \\ a_{m1} & \cdots & a_{mn} \end{bmatrix} = [\mathbf{u}_1 \cdots \mathbf{u}_k \cdots \mathbf{u}_n] \begin{bmatrix} s_{11} & 0 & 0 \\ 0 & \ddots & 0 \\ 0 & 0 & s_{nn} \end{bmatrix} \begin{bmatrix} \mathbf{v}_1 \\ \vdots \\ \mathbf{v}_k \\ \vdots \\ \mathbf{v}_n \end{bmatrix} \quad (\text{II-5})$$

After SVD, we have to decide on the number of significant components that are essential to reproduce matrix  $\mathbf{A}$ . Various criteria for deciding on the adequate number of SVD components are available in the literature. In one of those criteria, the contribution of each singular value to the whole data is evaluated and all of the singular values that account for 70–90% of the total of singular values are considered for reconstruction. In another criterion, singular values higher than the mean of all the singular values or higher than the fraction  $0.7/n$  ( $n$  denotes total number of singular values) are retained. However, these criteria may depend substantially on the noise level in the TRIR spectra. Furthermore, they tend to result in too many components, which make it impossible to analyze the time-resolved data using a physical model. Here we inspect spectral and temporal components ( $\mathbf{u}_k$  and  $\mathbf{v}_k$ ) of each singular value and focus on only components that exhibit physically meaningful spectral or temporal behaviors. By doing so, we can reduce noises and reproduce the matrix  $\mathbf{A}$  with a reasonably small number of components that typically account for more than 90% of the raw data.

## II-4 Global Fitting Analysis

Global fitting analysis [40] is a popular curve fitting technique used in time-resolved spectroscopic studies to check the validity of physical models used to explain experimental observations as well as to extract the spectral and dynamics information of the transient species generated in a photochemical reaction. We employed global fitting analysis in the Py/DCB work (see Chapter III). It performs simultaneous fitting of all the data using model functions with several common adjustable parameters. In time-resolved spectroscopy, the acquired spectra at different times are represented as a matrix. Let us denote such a matrix  $\mathbf{Y}$ . According to Beer–Lambert Law, the absorbance of the sample at wavelength  $\lambda$  and time  $t$ ,  $y(t, \lambda)$ , is the sum of contributions from all the absorbing species involved in the reaction. It can be expressed as follows:

$$\begin{aligned}
y(t, \lambda) &= c_1(t)\varepsilon_1(\lambda) + c_2(t)\varepsilon_2(\lambda) + c_3(t)\varepsilon_3(\lambda) + \dots + c_n(t)\varepsilon_n(\lambda) \\
&= \sum_{i=1}^n c_i(t)\varepsilon_i(\lambda)
\end{aligned}
\tag{II-6}$$

where  $c_i(t)$  is the concentration of the  $i$ th molecular species involved and  $\varepsilon_i(t)$  is the modified molar absorptivity of the same molecular species which is actually a product of path length ( $l$ ) and molar absorptivity ( $\varepsilon_i^\dagger(t)$ ). Hence matrix  $\mathbf{Y}$  can be very easily decomposed as shown in Eq. (II-7).

$$\mathbf{Y} = \mathbf{CS} + \mathbf{R} \tag{II-7}$$

where the columns of matrix  $\mathbf{C}$  represents the concentration profiles (i.e., time profiles) of transient species as a function of time, the rows of matrix  $\mathbf{S}$  represents the modified absorptivity of the transients (i.e., spectral profiles) as a function of wavelength, and  $\mathbf{R}$  represents the residual matrix, which in most cases represent random noises. An example of global fitting analysis is shown in Figure II-4. Hypothetical time-resolved spectra recorded at different time delays (Figure II-4a) are represented as a matrix. Here we use two components that obey first-order kinetics but show complementary behaviors so that the spectrum observed at any point in time and space can be represented as a linear combination of these two components alone. Using the fitting functions, all the waves are fit simultaneously. The concentration and spectral profiles obtained with global fitting are shown in Figure II-4b and Figure II-4c, respectively. The overall performance of the global fitting analysis can be examined by taking a closer look at the residuals shown in Figure II-4d. As there is no particular spectral/temporal pattern remaining except for noises, it is confirmed that the global fitting analysis is successful. A technical difficulty may arise when our starting physical model is exceedingly complex. Analytically solving rate equations is not always possible and hence we may need the help of numerical methods to perform this analysis.



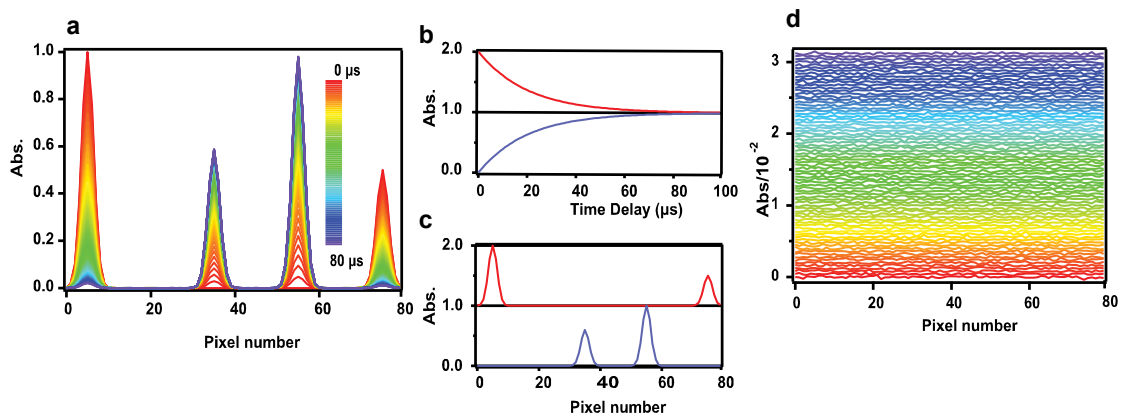
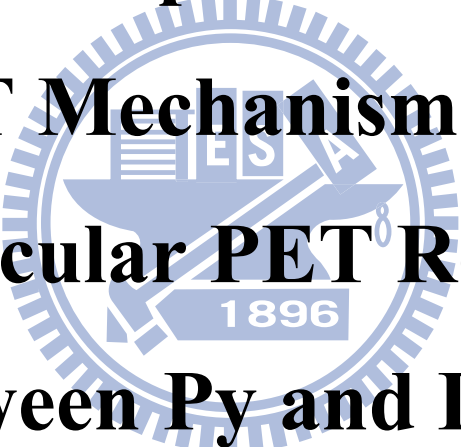


**Figure II-4.** Simulated time-resolved spectra (a), extracted concentration profiles (b), spectral profiles (c) and residuals (d) obtained after performing global curve fitting analysis over the time-resolved spectral data matrix shown in (a).



**Chapter III**  
**BET Mechanism of a**  
**Bimolecular PET Reaction**  
**between Py and DCB**



### III-1 Introduction

Photoinduced intermolecular electron transfer (PIET) reactions are one of the fundamentally important photochemical processes owing to its significance in photochemistry and photobiology [31,41,42]. PIET reactions play a prominent role in the function of OPVs. It is essential to advance our understanding of the PIET processes with a view to rational design of efficient devices that can solve the urgent issue of renewable energy sources. In a PIET, FET leads to charge formation, and BET leads to the decay of the induced charges via, e.g., recombination reactions. The latter process is strongly favored thermodynamically. Preventing or impeding the charge recombination seems to be an important prerequisite for enhancing the performance of DSSCs [43,44] as well as organic bulk heterojunction solar cells [45]. Although a variety of strategies have been developed and demonstrated, such as tuning the HOMO–LUMO band gap between the donor and the semiconductor material and changing orbital symmetry in donor–bridge–acceptor systems [46], efficient retardation of charge recombination is still a challenging goal in solar cell research.

The major obstacle to this goal arises from the fact that BET is very often not a simple recombination of primary charge carriers but a multistep photochemical reaction involving other molecular species in the system as well. Detailed understanding of the mechanism of BET is thus of paramount importance for overcoming the conundrum of fast charge recombination in all photovoltaic devices. Spectroscopic approaches provide a direct means to look at PET reactions and have proven powerful for such mechanistic studies. Much work using transient absorption spectroscopy has focused on ultrafast FET reactions [47-52]. Hino et al. [53,54] provided a detail account on the mechanism of FET by using Py–*N,N*-dimethyl aniline (DMA) and Py–DCB systems. They found that FET in Py–DMA proceeds through formation of an exciplex in moderately polar solvents followed by formation of contact ion pairs, solvated ion pairs, and free ions. In Py–DCB, however, FET proceeds through solvated ion pairs and free ions. No exciplex formation has been detected in this system. Though the energies of exciplexes, solvated ion pairs and free ions are similar for both Py–DMA and Py–DCB systems, the FET pathways are different. They also worked on various Py–quencher systems [53], where the quencher can be either a donor or an acceptor, and found that there is no correlation between electron donor–acceptor interactions and the photodissociation yields of free ions. They concluded that the chemical property of the quencher is a key to understanding FET mechanism. Koch et al. [55] detected the formation of exciplexes in PIET reactions using ultrafast IR spectroscopy. Ultrafast transient absorption and IR spectroscopies

[56,57] have been used to detect both contact ion pairs and solvated ion pairs in PIET reactions.

In contrast to FET, BET reactions, which proceed on a much slower time scale (typically in the ns– $\mu$ s time regime), are yet to be more thoroughly investigated in particular with regard to their reaction mechanisms. In this study, we used time-resolved NIR and MIR spectroscopy [12,58] to unveil the mechanism of the BET dynamics in the PIET reaction between Py and DCB dissolved in ACN. Unlike conventional transient absorption spectroscopy, our technique is able to detect vibrational transitions in the MIR region as well as specific types of electronic transition (e.g., CT transitions) that appear in the NIR region, making it feasible to identify and distinguish between coexisting molecular species.

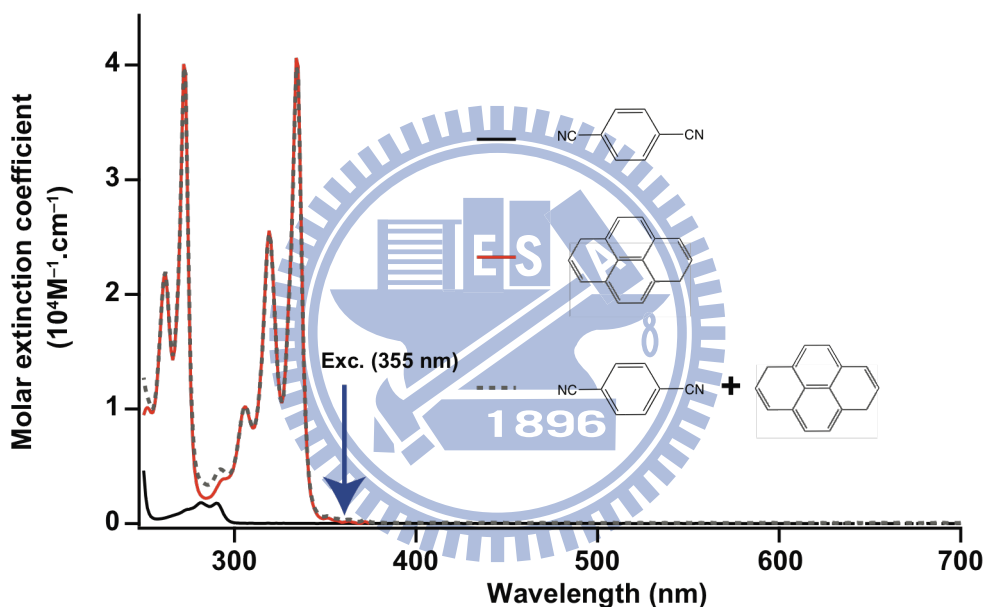


**Figure III–1.** UV/Vis spectra of Py (red solid curve) and DCB (black solid curve) in ACN solution. Also shown is the UV/Vis spectrum of the ACN solution of both Py and DCB (grey dashed curve). In all solutions, the concentrations of Py and DCB were 0.50 and 5.0 mM, respectively. The molar extinction coefficient of Py at the excitation wavelength (355 nm) is  $280 \text{ M}^{-1} \text{ cm}^{-1}$ , whereas that of DCB is one order of magnitude smaller.

Py and DCB form a fundamental PIET system [54,59-61] suitable for the mechanistic study of BET. Upon photoexcitation of Py in the presence of DCB in polar solvent (see Figure III–1 for the UV/Vis spectra of Py and DCB in ACN), Py radical cation ( $\text{Py}^{\bullet+}$ ) and DCB radical anion ( $\text{DCB}^{\bullet-}$ ) are produced within 100 ns via intermolecular electron transfer from the  $\text{S}_1$  state of Py. The efficiency of FET reaction is expected to be considerable owing to the same LUMO symmetry of Py and DCB [62,63], which is reflected in the quantum

yields of ion pairs ( $\Phi_{ip} = 0.38$  in ACN ( $\epsilon = 37.5$ ) and  $0.08$  in dichloromethane ( $\epsilon = 3.75$ )). Surrounding polar solvent molecules usually stabilize the generated ionic species and keep these ions apart. As a result, the generated ionic species become free ions. Thus the recombination of ion pairs is anticipated to occur at a slower rate of  $10^4$ – $10^5$  s<sup>-1</sup>, since the diffusion rate constant is of the order of  $10^{10}$  M<sup>-1</sup> s<sup>-1</sup> and the concentration of ions generated is of the order  $10^{-5}$ – $10^{-6}$  M. The focus of this work is on this slower dynamics of the free ions during which an electron is back-transferred and the ions are brought to the neutral state. This process in the Py–DCB system may be viewed as mirroring the dye regeneration by the iodide/triiodide redox couple in standard DSSCs [64-66]. The analogy here is not rigorous in the sense that dye regeneration in DSSCs is a part of sequential “forward” transfer reactions and not really “back” electron transfer. Nevertheless, as will be shown below, the BET in the Py–DCB system seems to resemble closely the process of the dye regaining an electron from anionic species in DSSC solvent.

## III-2 Materials and Methods

### III-2.1 Materials

Py ( $\geq 99\%$ ) and DCB (98%) were purchased from Sigma Aldrich. HPLC-grade ACN was purchased from J. T. Baker. Prior to spectroscopic measurements, Py and DCB were purified by sublimation and subsequent recrystallization from ethanol (anhydrous). ACN was used as received. Py and DCB were dissolved in ACN at 0.50 and 5.0 mM, respectively.

### III-2.2 Nanosecond Time-resolved Near/Mid-IR Spectroscopy

The laboratory-built nanosecond TRIR spectrometer used in the present study has been described in Chapter II. A 355 nm pulse (7 ns duration; 36  $\mu$ J energy; 500 Hz repetition rate) photoexcited Py in the sample solution, which was continuously circulated by a gear pump through a 500  $\mu$ m flow cell consisting of two CaF<sub>2</sub> windows. The sample solution in the reservoir was normally bubbled with argon gas. In the oxygen quenching experiment, however, it was saturated with oxygen gas. The spectral resolution was set to 200 cm<sup>-1</sup> for the NIR and 16 cm<sup>-1</sup> for the MIR. The FTIR spectrum of Py in CD<sub>3</sub>CN (Figure III–3a) was recorded on a JASCO FT/IR-6100 spectrometer using a sample cell composed of two CaF<sub>2</sub> windows and a 100- $\mu$ m lead spacer. A spectral resolution of 2 cm<sup>-1</sup> was used in the FTIR measurement. All measurements were performed at room temperature.

### III-2.3 Computational Details

DFT calculations of isolated Py monomer and Py dimer cation ( $\text{Py}_2^{*+}$ ) were carried out with the B3LYP exchange-correlation functional [67,68] in conjunction with empirical dispersion correction recently introduced by Grimme and co-workers [69] (B3LYP-D3). The aug-cc-pVTZ basis set [70,71] was adopted in this work. Equilibrium geometries, harmonic vibrational frequencies, and IR intensities were determined using Gaussian 09 program package [72]. To facilitate comparison with experimental IR spectra, calculated harmonic frequencies were uniformly scaled by a factor of 0.97 in accordance with a reported B3LYP/aug-cc-VDZ scaling factor of 0.9698 for frequencies higher than  $1000\text{ cm}^{-1}$ . Theoretical IR spectra were plotted using a Gaussian band envelop with a full-width at half-maximum (FWHM) of  $10\text{ cm}^{-1}$ . All computational work was done by Dr. Yoshifumi Nishimura and Prof. Henryk A. Witek.

## III-3 Results and Discussion

### III-3.1 Nanosecond TRNIR/MIR Spectra of Py and DCB in ACN Solution Measured under Ar Bubbling.

In this section, results of nanosecond TRIR spectroscopy of the BET reaction in the Py–DCB system are presented. TRNIR/MIR spectra of Py and DCB in ACN show four prominent transient absorption bands (Figure III–2a–c) with maxima at  $6800$ ,  $2100$ ,  $1216$ , and  $1136\text{ cm}^{-1}$  and a very broad feature that extends from  $\sim 9000\text{ cm}^{-1}$  toward the visible. The temporal behaviors of the five transient features are displayed in Figure III–2d–h. All of these time profiles have an instantaneous rise except for the transient at  $11000\text{ cm}^{-1}$  (Figure III–2d), which exhibits a somewhat slower rise compared with the other transients. The decay kinetics of the transients at  $11000$ ,  $6800$ ,  $1216$ , and  $1136\text{ cm}^{-1}$  (Figure III–2,e,g,h) appear similar, but, interestingly, they are quite different from that of the transient at  $2100\text{ cm}^{-1}$  (Figure III–2f). Because the FET reaction is complete within the time resolution of the apparatus ( $\sim 80\text{ ns}$ ) [61], the transient bands we observed must be predominantly due to either  $\text{Py}^{*+}$  or  $\text{DCB}^{*-}$ . However  $\text{Py}^{*+}$  is known to form  $\text{Py}_2^{*+}$  via interacting with Py in a diffusion controlled manner [73,74]. Thus  $\text{Py}_2^{*+}$  may also occur along with  $\text{Py}^{*+}$  in the solution. It is well established that  $\text{Py}_2^{*+}$  [73,75,76] shows a charge-resonance electronic band at around  $6700\text{ cm}^{-1}$  in polar solvent, so the NIR band at  $6800\text{ cm}^{-1}$  can be unambiguously assigned to  $\text{Py}_2^{*+}$ . The two MIR

bands at 1216 and 1136  $\text{cm}^{-1}$  are vibrational bands originating also from  $\text{Py}_2^{*+}$  because they appear to decay synchronously with the charge-resonance band of  $\text{Py}_2^{*+}$ .

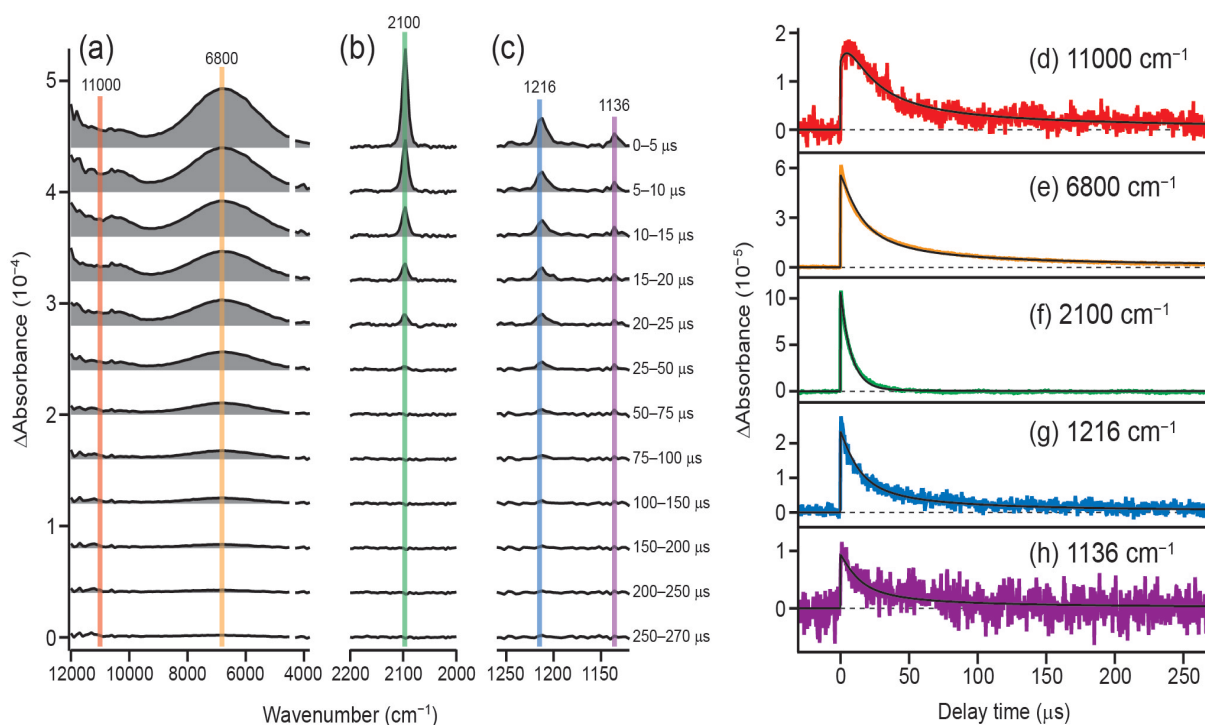


**Figure III-2.** Left: Time-resolved IR spectra in the regions 3800–12000  $\text{cm}^{-1}$  (a), 2000–2200  $\text{cm}^{-1}$  (b), and 1120–1260  $\text{cm}^{-1}$  (c), of Py and DCB dissolved in ACN (0.50 and 5.0 mM, respectively) excited at 355 nm with Ar bubbling. The spectra in (a) are masked at around 4400  $\text{cm}^{-1}$  due to an overtone band of the solvent. Each time-resolved spectrum is offset by  $4 \times 10^{-5}$  for clarity of display. Right: Time profiles at 11000 (d), 6800 (e), 2100 (f), 1216 (g), and 1136 (h)  $\text{cm}^{-1}$ . The smooth black curves are the result of the kinetic analysis based on the reaction mechanism shown in Scheme III-1.

### III-3.2 Vibrational Assignments

In this section, the vibrational assignments of the transient species observed in the TRIR spectra are discussed. To assign these vibrational bands, we refer to DFT calculation results of gas-phase Py and  $\text{Py}_2^{*+}$ . The FTIR spectrum of Py in ACN (Figure III-3a) shows three prominent bands at 1244, 1186, and 1096  $\text{cm}^{-1}$ , which are well reproduced in the calculated IR spectrum (Figure III-3b) at 1235, 1182, and 1088  $\text{cm}^{-1}$ , respectively.

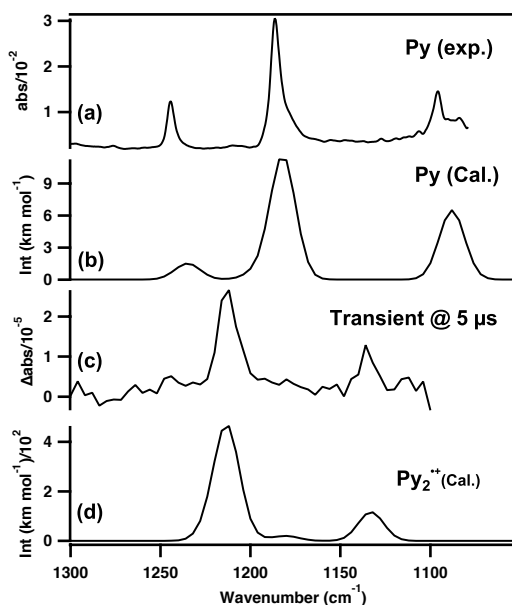


**Figure III-3.** (a) FTIR spectrum of Py (30 mM) in CD<sub>3</sub>CN. (b) DFT/B3LYP calculated IR spectrum of the gas phase Py molecule (plotted using a Gaussian band envelop with a FWHM of 10 cm<sup>-1</sup>). (c) Transient IR spectrum at 0–5 μs, same as the top trace of Figure III-1c. (d) DFT/B3LYP calculated IR spectrum of gas phase Py<sub>2</sub><sup>++</sup>.

Remarkably, the calculated spectrum of Py<sub>2</sub><sup>++</sup> is also in excellent agreement with experiment. The observed transient MIR spectrum at 0–5 μs (Figure III-3c; same as the top trace of Figure III-2c) shows perfect spectral resemblance with the calculated IR spectrum of Py<sub>2</sub><sup>++</sup> (Figure III-3d). The calculation reveals three IR bands at 1213, 1195, and 1133 cm<sup>-1</sup> (Figure III-3d), of which the 1213 and 1133 cm<sup>-1</sup> bands are likely to correspond to the two transient bands at 1216 and 1136 cm<sup>-1</sup> (Figure III-3c). These bands are assigned to C–H in-plane bending and in-plane ring deformation, respectively. The discrepancy in frequency between experiment and theory is found to be only –3 cm<sup>-1</sup>. The calculated band at 1195 cm<sup>-1</sup> is not clearly seen in the experimental spectrum because of poor S/N, but we could see a small hump at the red edge of the intense 1213 cm<sup>-1</sup> band and it might correspond to the calculated band at 1195 cm<sup>-1</sup>.

The DFT calculations suggest that the contribution of Py<sup>++</sup> is relatively small because the calculated IR spectrum of Py<sup>++</sup> (data not shown) is in less agreement with experiment than that of Py<sub>2</sub><sup>++</sup>. This conclusion can also be justified as follows. The ionic species of polycyclic aromatic hydrocarbons tend to dimerize in solution and dimer cations are energetically more favored than their monomer counterparts [75,77,78]. In addition to the difference in population, the reactivity of monomeric species are faster than dimeric species by an order of magnitude [74,75]. Nevertheless, we find no noticeable difference in decay kinetics between



the 6800  $\text{cm}^{-1}$  band ( $\text{Py}_2^{++}$ ) and the 1216 and 1136  $\text{cm}^{-1}$  bands. Considering all these together, the negligible contribution of  $\text{Py}^{++}$  in the measured spectra seems reasonable.

The 2100  $\text{cm}^{-1}$  band is characteristic of the  $\text{C}\equiv\text{N}$  stretching mode of nitriles and is safely attributable to  $\text{DCB}^{\bullet-}$ . Our DFT/B3LYP calculation of gas-phase  $\text{DCB}^{\bullet-}$  indeed predicts a very intense IR band at 2112  $\text{cm}^{-1}$  (data not shown), in excellent agreement with the observed peak position. This band arises from the asymmetric combination of the two  $\text{C}\equiv\text{N}$  stretches. Thus we have successfully assigned all the vibrational bands observed in the TRIR spectrum using DFT/B3LYP calculations.

### III-3.3 Molecular Oxygen Quenching Experiment

So far, all the transient bands have been assigned except for the spectral features over 9000  $\text{cm}^{-1}$  that can be associated with neither  $\text{Py}_2^{++}$  nor  $\text{DCB}^{\bullet-}$ . In this section, the experimental results of  $\text{O}_2$  quenching experiments performed by bubbling the solution with  $\text{O}_2$  are presented to obtain a clue to the origin of the spectral features over 9000  $\text{cm}^{-1}$ .

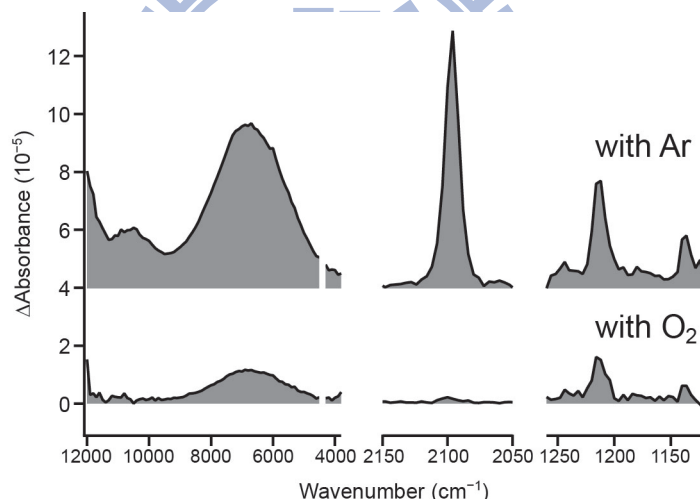


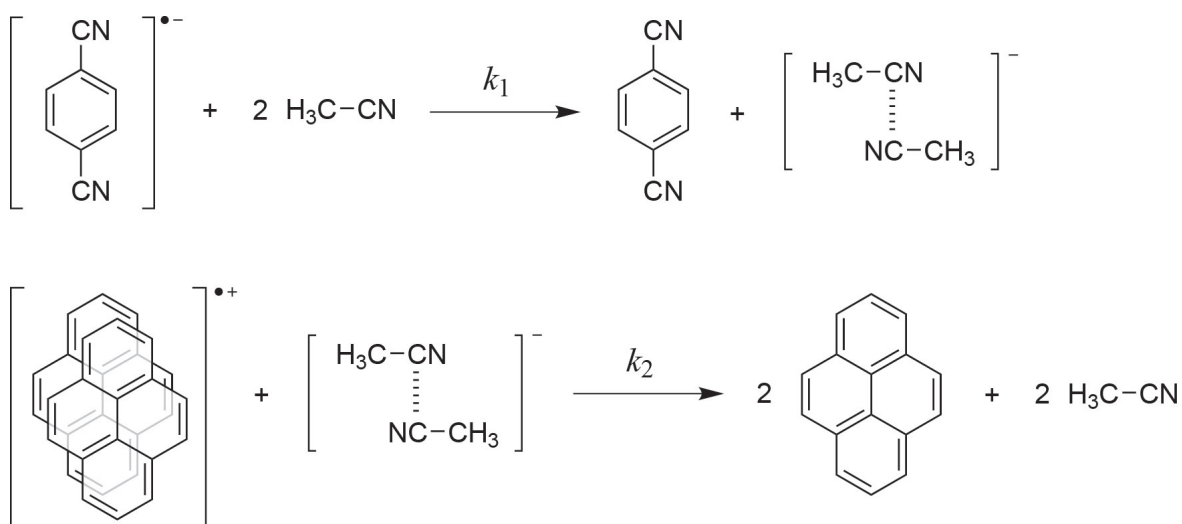
**Figure III-4.** Time-resolved near- and mid-IR spectra of Py (0.50 mM) and DCB (5.0 mM) dissolved in ACN, measured at 0–5  $\mu\text{s}$  with Ar (top) and  $\text{O}_2$  (bottom) bubbling. The spectrum taken with Ar bubbling is offset by  $4 \times 10^{-5}$  for clarity of display.

Anions are usually more efficiently quenched by molecular oxygen than cations. The intensities of the transient bands at 11000 and 2100  $\text{cm}^{-1}$  are drastically quenched with oxygen bubbling (Figure III-4, bottom) to an almost undetectable level compared with those at 6800, 1216, and 1136  $\text{cm}^{-1}$  (Figure III-4, top). The overall intensity drop in the transient spectra is attributable to the quenching of the excited-state population [79,80]. This result indicates that the transient band at 11000  $\text{cm}^{-1}$  comes from an anionic species. The 11000

$\text{cm}^{-1}$  transient could be produced as a result of reaction between  $\text{DCB}^{\bullet-}$  and solvent ACN, considering the strong electron affinity of ACN. The electron affinity of ACN in vacuum is  $-2.84$  eV [81] and forms solvent anions [81-83] via reactions of an excess electron with one or more ACN molecules, along with the stabilization of an excess electron ejected in ACN by a substantial solvent shell. Those reactions would result in the formation of  $\text{ACN}_n^-$  (“traditional” solvated electron) [81-83]. Previous studies [84,85] on ejection of excess electron in ACN found two species with absorption bands in the visible ( $\sim 530$  nm) and NIR regions ( $\sim 1500$  nm). The lower-energy electronic band in the NIR region has been assigned to dipole bound solvated electron. However, the reported lifetime of the solvated electron in ACN ( $\sim 80$  ps) [84,85] is simply too short to be detected with our apparatus. The higher-energy electronic band in the visible region has been assigned to ACN dimer anion  $\text{ACN}_2^-$ , in which the excess electron forms a covalent bond between the cyano-carbons of two antiparallel ACN molecules. The assignment of  $\text{ACN}_2^-$  is thoroughly corroborated based on transient absorption [84,85],  $\gamma$ -radiolysis of  $\alpha$ -ACN at 77 K [83], and theoretical calculations [81-83,86]. From the previous study of Shkrob et al. [84,85], it is known that  $\gamma$ -radiolysis of two crystalline forms of ACN (namely, monoclinic  $\alpha$ -ACN and orthorhombic  $\beta$ -ACN) produces  $\text{ACN}_2^-$  and  $\text{ACN}^-$  with bands at 530 and 420 nm, respectively. The possibility of  $\text{ACN}^-$  is ruled out in liquid ACN based on the stability of neutral dimers and the molecular orientation in liquid ACN that should be close to  $\alpha$ -ACN. It is thus very likely that the higher-energy band in the visible region is assigned to  $\text{ACN}_2^-$ , whose red edge has been observed in the present study, and we attribute the spectral feature above  $9000$   $\text{cm}^{-1}$  to  $\text{ACN}_2^-$ .

### III-3.4 Kinetic Analysis

Having assigned the five transient bands to  $\text{Py}_2^{\bullet+}$ ,  $\text{DCB}^{\bullet-}$ , and  $\text{ACN}_2^-$ , we now examine their time profiles (Figure III-2d-h) in more depth. The observation that  $\text{Py}_2^{\bullet+}$  and  $\text{DCB}^{\bullet-}$  show markedly different decay kinetics (compare, e.g., Figure III-2e,f) seems counter-intuitive because it is compelling to think that those carriers with opposite charges should decay in unison, irrespective of whether geminate (first-order reaction) or non-geminate (second-order reaction) recombinations take place, in order to maintain charge balance.



**Scheme III-1.** Top:  $\text{DCB}^{\bullet-}$  ejects an electron into the solvent ACN, resulting in the formation of neutral DCB and  $\text{ACN}_2^{\bullet-}$ . Bottom:  $\text{Py}_2^{\bullet+}$  captures the excess electron in  $\text{ACN}_2^{\bullet-}$ .

To account for the observed asynchronous decay kinetics in the Py–DCB system, we propose here a mechanism of the BET reaction between  $\text{Py}_2^{\bullet+}$  and  $\text{DCB}^{\bullet-}$  in which ACN plays a pivotal role as a charge mediator (Scheme III-1). There are two possible decay channels for  $\text{DCB}^{\bullet-}$ : (1) the recombination with  $\text{Py}_2^{\bullet+}$  and (2) ejection of the electron into the solvent leading to the formation of  $\text{ACN}_2^{\bullet-}$  (Scheme III-1, top). In case 1,  $\text{DCB}^{\bullet-}$  would decay concurrently with  $\text{Py}_2^{\bullet+}$ . The observed time profiles contradict this prediction, suggesting that case 2, i.e., the electron ejection into the solvent, is the major route of the  $\text{DCB}^{\bullet-}$  decay. It follows a pseudo-first-order reaction with rate constant  $k_1'$  ( $= k_1[\text{ACN}]^2$ ). The preference for the electron ejection into ACN over the  $\text{Py}_2^{\bullet+}/\text{DCB}^{\bullet-}$  recombination may well be due to several factors, such as orbital symmetry mismatch between the HOMO of Py and the LUMO of DCB [62,63], the high capability of ACN to solvate electrons, and the abundance of ACN as solvent molecules ( $[\text{Py}]:[\text{DCB}]:[\text{ACN}] = 1:10:40000$ ). The formation of  $\text{ACN}_2^{\bullet-}$  is clearly manifested as the initial rise of the transient at  $11000\text{ cm}^{-1}$  with a maximum at  $\sim 6\text{ }\mu\text{s}$  (see Figure III-2d). Because  $\text{DCB}^{\bullet-}$  decays preferentially via the reaction with ACN, the only available decay pathway for  $\text{Py}_2^{\bullet+}$  that retains charge neutrality of the system is the interaction with  $\text{ACN}_2^{\bullet-}$ , which obeys a second-order rate law with rate constant  $k_2$  (Scheme III-1, bottom).

The resulting rate equations governing the kinetics of the system are given by

$$\frac{d[\text{DCB}^{\bullet-}]}{dt} = -k_1' [\text{DCB}^{\bullet-}] \quad (\text{III-1})$$

$$\frac{d[\text{Py}_2^{\bullet+}]}{dt} = -k_2 [\text{Py}_2^{\bullet+}][\text{ACN}_2^{\bullet-}] \quad (\text{III-2})$$

$$\frac{d[\text{ACN}_2^{\bullet-}]}{dt} = k_1' [\text{DCB}^{\bullet-}] - k_2 [\text{Py}_2^{\bullet+}][\text{ACN}_2^{\bullet-}] \quad (\text{III-3})$$

By solving Eqs. (III-1)–(III-3) with the initial conditions  $[\text{Py}_2^{*\cdot+}] = [\text{DCB}^{\cdot-}] = C_0$  and  $[\text{ACN}_2^-] = 0$  at  $t = 0$  and with the charge neutrality condition  $[\text{Py}_2^{*\cdot+}] = [\text{DCB}^{\cdot-}] + [\text{ACN}_2^-]$  at any given time  $t$ , we are able to obtain the time-dependent changes in the concentrations of  $\text{Py}_2^{*\cdot+}$  and  $\text{DCB}^{\cdot-}$  as follows:

$$[\text{DCB}^{\cdot-}] = C_0 \exp(-k_1' t) \quad (\text{III-4})$$

$$[\text{Py}_2^{*\cdot+}] = \frac{C_0 \exp[\alpha(1 - \exp(-k_1' t))]}{1 + \alpha \exp(\alpha)[\text{Ei}(-\alpha) - \text{Ei}(-\alpha \exp(-k_1' t))]} \quad (\text{III-5})$$

where  $\alpha = C_0 k_2 / k_1'$  and  $\text{Ei}(x)$  represents the exponential integral defined as  $\text{Ei}(x) = \int_{-\infty}^x e^t / t dt$ .

These solutions can be verified by substitution of Eqs. (III-4) and (III-5) into Eqs. (III-1) and (III-2). The IR absorbance difference at time  $t$  and wavenumber  $\tilde{\nu}$ ,  $\Delta A(\tilde{\nu}, t)$ , can be expressed as a linear combination of  $[\text{DCB}^{\cdot-}]$ ,  $[\text{Py}_2^{*\cdot+}]$ , and  $[\text{ACN}_2^-]$ :

$$\Delta A(\tilde{\nu}, t) = a_1(\tilde{\nu})[\text{DCB}^{\cdot-}] + a_2(\tilde{\nu})[\text{Py}_2^{*\cdot+}] + a_3(\tilde{\nu})[\text{ACN}_2^-] \quad (\text{III-6})$$

where  $a_1(\tilde{\nu})$ ,  $a_2(\tilde{\nu})$ , and  $a_3(\tilde{\nu})$  represent the amplitudes of the time-dependent concentrations of  $\text{DCB}^{\cdot-}$ ,  $\text{Py}_2^{*\cdot+}$ , and  $\text{ACN}_2^-$ , respectively. Due to the charge neutrality condition, Eq. (III-6) leads to

$$\begin{aligned} \Delta A(\tilde{\nu}, t) &= a_1(\tilde{\nu})[\text{DCB}^{\cdot-}] + a_2(\tilde{\nu})[\text{Py}_2^{*\cdot+}] + a_3(\tilde{\nu})([\text{Py}_2^{*\cdot+}] - [\text{DCB}^{\cdot-}]) \\ &= b_1(\tilde{\nu})[\text{DCB}^{\cdot-}] + b_2(\tilde{\nu})[\text{Py}_2^{*\cdot+}] \end{aligned} \quad (\text{III-7})$$

with  $b_1(\tilde{\nu}) = a_1(\tilde{\nu}) - a_3(\tilde{\nu})$  and  $b_2(\tilde{\nu}) = a_2(\tilde{\nu}) + a_3(\tilde{\nu})$ .

To test the validity of our model we performed a global curve fitting analysis of the time-resolved spectra shown in Figure III-2a–c using Eq. (III-7) together with Eqs. (III-4) and (III-5). The parameters used in the fitting are the amplitudes of the two contributions  $[\text{Py}_2^{*\cdot+}]$  and  $[\text{DCB}^{\cdot-}]$  in the linear combinations (i.e.,  $b_1$  and  $b_2$  in Eq. (III-7)),  $k_1'$ , and  $\alpha$ . The global analysis yields  $k_1' = (1.1 \pm 0.2) \times 10^5 \text{ s}^{-1}$  and  $\alpha = 0.4 \pm 0.1$ . The smooth curves in Figure III-2d–h are best fits obtained with these parameters, from which it is clear that the kinetic analysis based on our proposed reaction mechanism (Scheme III-1) could successfully reproduce the observed time profiles of the five transient bands. A good agreement between experiment and simulation is also found in the entire spectral window studied, as shown in Figure III-5.

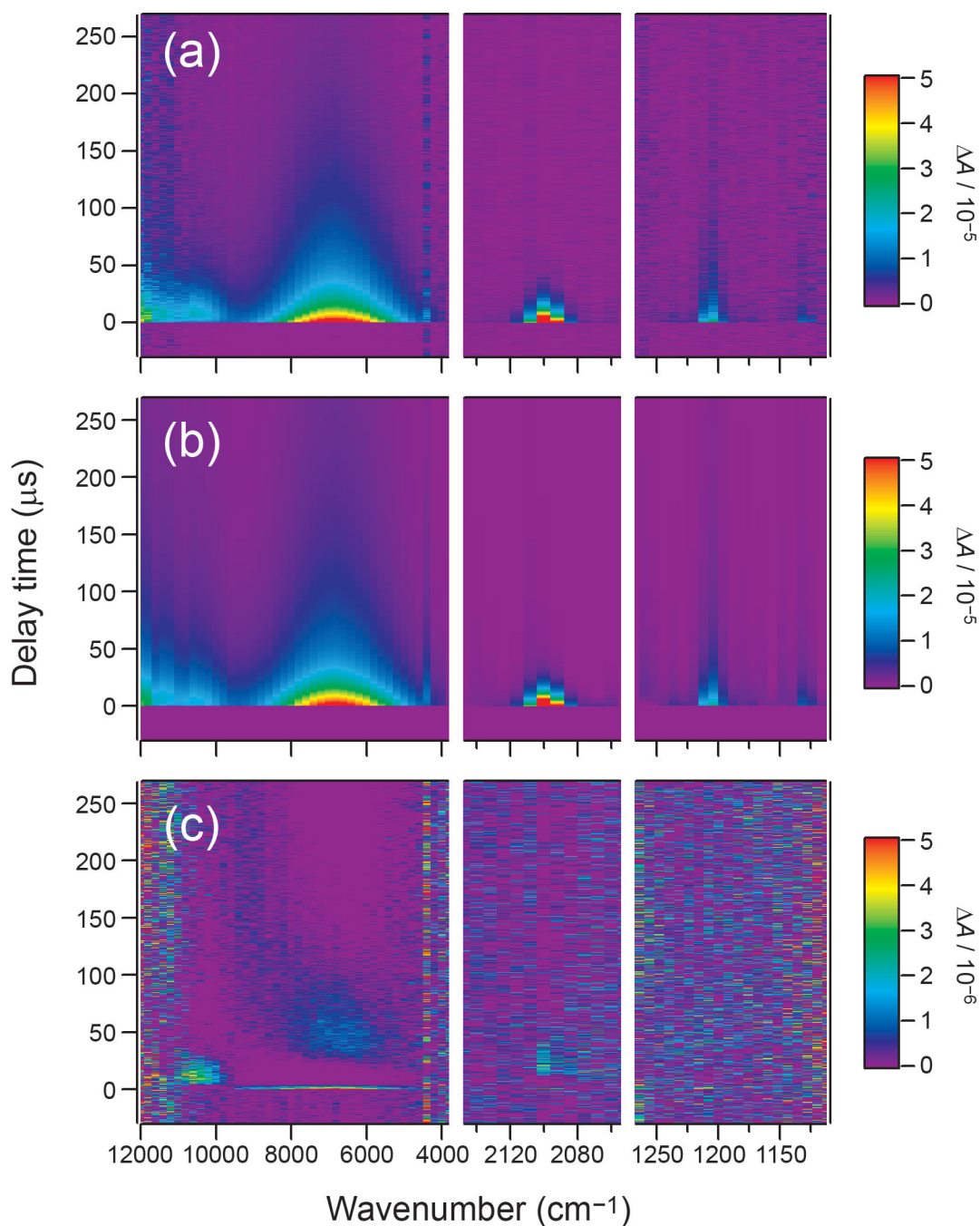


**Figure III-5.** Two-dimensional (2D) plots of the observed time-resolved spectra (a), the fitted result (b), and the residue (c). Each of the three 2D plots is represented in a rainbow pseudo color scale: the highest  $\Delta A$  value appears red and the lowest appears purple. Note that the maximum  $\Delta A$  value is  $5 \times 10^{-5}$  in (a) and (b) and  $5 \times 10^{-6}$  in (c).

The above global fitting alone does not allow us to determine  $C_0$  and  $k_2$  independently, because they appear together as parameter  $\alpha$  in the fitting functions (see Eqs. (III-4) and (III-5)). However, we are able to provide estimates for the values of  $C_0$  and  $k_2$ . Approximately 1% of Py molecules are calculated to be photoexcited under the present excitation conditions, so

the upper limit of the initial concentration  $C_0$  is  $5 \times 10^{-6}$  M. Given the reported quantum yield of 0.38 of the ion-pair ( $\text{Py}_2^{++}$  and  $\text{DCB}^{\bullet-}$ ) formation in ACN [54], the value of  $C_0$  is most likely of the order of  $10^{-6}$  M, resulting in  $k_2 \approx 10^{10} \text{ M}^{-1} \text{ s}^{-1}$ .

### III-3.5 Concentration Dependence Studies of the BET Reaction between Py and DCB in ACN Solution

In this section, concentration dependence of the BET reaction between Py and DCB is examined. As the formation of  $\text{Py}_2^{++}$  and recombination reaction between  $\text{Py}_2^{++}$  and  $\text{ACN}_2^-$  are both second-order reactions, diffusion plays a prominent role. Thus it will be useful to test the proposed reaction scheme (refer to Section III-3.4) at various different concentrations. We measured TRNIR/MIR spectra of 5.0 mM Py and 5.0 mM DCB, where the concentration of Py was increased by one-fold and that of DCB was kept the same. Lowering the concentration of Py or DCB was not feasible as the intensity of the vibrational bands recorded at 0.5 mM Py and 5.0 mM DCB are close to the detection limit of the present apparatus.

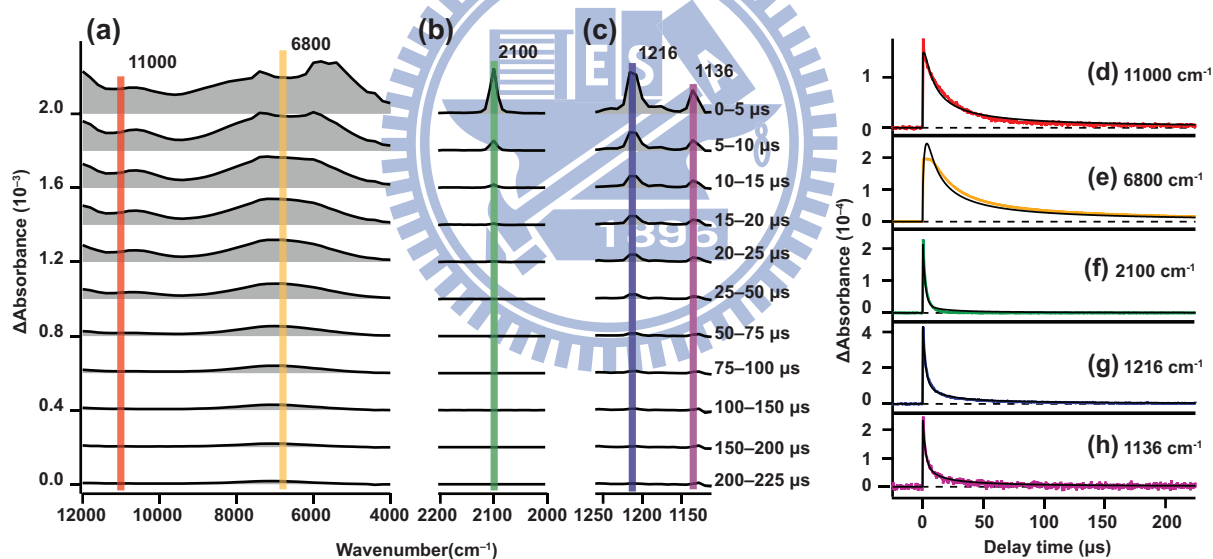


**Figure III-6** Left: Time-resolved IR spectra in the regions  $3800\text{--}12000 \text{ cm}^{-1}$  (a),  $2000\text{--}2200 \text{ cm}^{-1}$  (b), and  $1120\text{--}1260 \text{ cm}^{-1}$  (c), of Py and DCB dissolved in ACN (5.0 and 5.0 mM, respectively) excited at 355 nm with Ar bubbling. Each time-resolved spectrum is offset by  $2 \times 10^{-4}$  for clarity of display. Right: Time profiles at 11000 (d), 6800 (e), 2100 (f), 1216 (g), and 1136 (h)  $\text{cm}^{-1}$ . The smooth black curves are the result of the kinetic analysis based on the reaction mechanism shown in Scheme III-1.

The TRNIR/MIR spectra recorded at the higher concentrations of Py and DCB (Figure III-6) display similar spectral features to those of the transients observed at lower

concentrations (Figure III-2). However, there are appreciable differences in terms of band intensity and shape. The intensity ratio of the  $2100\text{ cm}^{-1}$  band to the 1216, 1136, and  $11000\text{ cm}^{-1}$  bands increases compared to the lower Py-concentration experiment. This increase could be due to the increase in the concentration of  $\text{Py}_2^{*\dagger}$  relative to  $\text{ACN}_2^-$ . In addition, the NIR transient at  $\sim 7000\text{ cm}^{-1}$  exhibits two peaks at  $\sim 7400$  and  $\sim 6000\text{ cm}^{-1}$ . This change in the band shape of the electronic band of  $\text{Py}_2^{*\dagger}$  could be due to the occurrence of a side reaction that is not taken into account in Scheme III-1. The concentration dependence is more evident in the kinetic behavior of the transients (Figure III-6 d, e, f, g and h). The  $6800\text{ cm}^{-1}$  band (Figure III-6e) shows a slower rise compared with the other transients (Figure III-6 d, f, g and h) at the higher Py concentration than at the lower concentration (Figure III-2e). The synchronous decay seen for the  $6800$ ,  $1216$ , and  $1136\text{ cm}^{-1}$  bands at the lower concentration (Figure III-2e, g and h) is no longer observed at the higher concentration (Figure III-6e, g and h). At the higher Py concentration, BET appears to proceed through a different scheme. To confirm this, a global fitting analysis is performed on the kinetic traces of the transients using Scheme III-1. The reaction scheme is found to fail to reproduce the experimental data, strongly suggesting that a different scheme should apply at the higher Py concentration. The BET reaction mechanism that can account for the TRNIR/MIR spectra at  $5.0\text{ mM}$  Py and  $5.0\text{ mM}$  DCB needs further investigation.

### III-3.6 TRIR Spectra of Py and DCB in Benzene Solution

In the earlier sections, we have shown that the unique ability of ACN to solvate electrons dictates the BET dynamics between Py and DCB. It would be natural to expect that the entire picture would be changed drastically in different solvents. To show that this is really the case, we measured TRIR spectra of Py and DCB in benzene (Figure III-7).

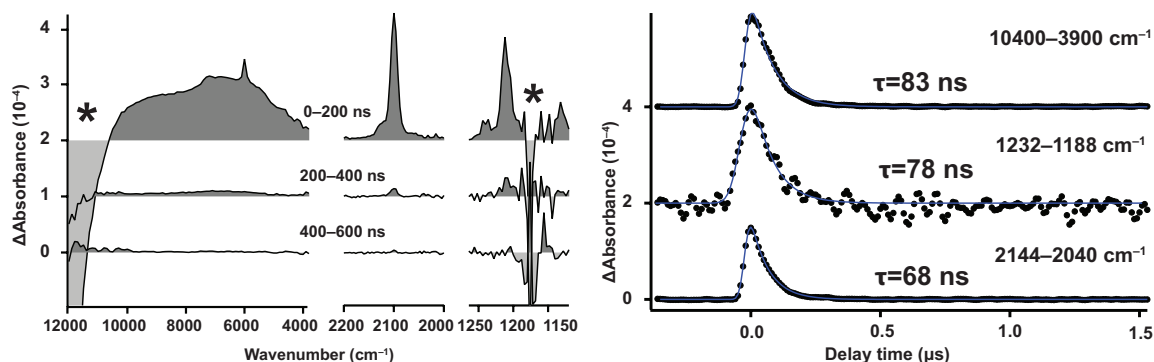


**Figure III–7.** Left: Time-resolved near- and mid-IR spectra of Py (5.0 mM) and DCB (50 mM) dissolved in benzene, excited at 355 nm with argon bubbling. Each spectrum is offset by  $1 \times 10^{-4}$  for clarity of display. Asterisks indicate an interference from a solvent band in the mid-IR region and a bleach due to the stimulated emission of Py in the near-IR region. Right: Averaged time profiles of the transient bands between 10400–3900, 1232–1188 and 2144–2040  $\text{cm}^{-1}$  (dots). The smooth curves are fits to an exponential function convolved with a Gaussian instrumental response function.

In sharp contrast to the ACN case, the decay of the transients seen in Figure III–7 is extremely fast and completes within 500 ns. The time profiles of the transient bands are shown on the right side of Figure III–7. The exponential time constants of these time profiles are close to the time resolution of the apparatus ( $\sim 80$  ns). Additionally, the NIR transient in benzene shows a much broader absorption with some structure on it than  $\text{Py}_2^{*+}$  in ACN (see Figure III–2a). These observations suggest that the BET in benzene occurs via a different mechanism such as direct recombination of  $\text{Py}^{*+}$  and  $\text{DCB}^{*-}$ .

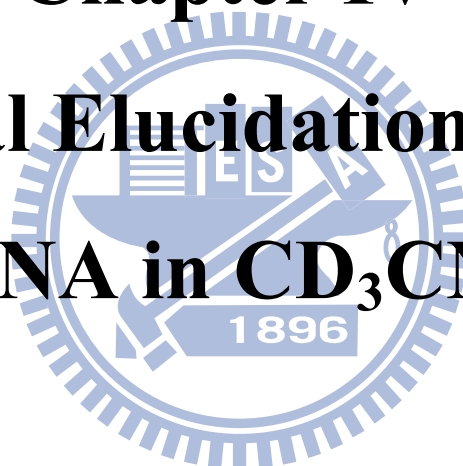
### III-4 Summary

We have shown that the reaction mechanism we propose (Scheme III–1) accounts well for the experimental results, in particular the asynchronous decay of  $\text{Py}_2^{*+}$  and  $\text{DCB}^{*-}$ . We have revealed a dual role of ACN as solvent and a reactant that mediates BET from  $\text{DCB}^{*-}$  to  $\text{Py}_2^{*+}$ . The reaction mechanism we proposed is one of the simplest mechanisms with a minimum set of parameters that one could think of. To our knowledge, this study is the first to provide such a detailed account on the dynamics of BET reactions. Our conclusion that ACN is a key player in the BET reaction involving the relevant dye will call new attention to the importance of the solvent for optimizing DSSCs' photovoltaic performance.



# **Chapter IV**

## **Structural Elucidation on the T<sub>1</sub> State of PNA in CD<sub>3</sub>CN Solution**



## IV-1 Introduction

PNA is a prototypical push-pull chromophore with the electron withdrawing NO<sub>2</sub> group at one end and the electron donating NH<sub>2</sub> group on the other end joined by a benzene ring. PNA exhibits a large first-order hyperpolarizability [87-94] and is well known for its nonlinear optical properties with possible applications in electro-optic and second harmonic generation materials. Photophysical properties of this compound have been studied both experimentally [35,87,95-103] and theoretically [104-108]. In particular, attempts have been made to understand the nature of the low-lying excited states that are pivotal in characterizing the optical properties of PNA. Raman spectra of PNA have been measured under non-resonance, pre resonance and resonance conditions in various solvents [87,96,100,101]. It is found that changing the solvent affects the excited state more than the ground state [93]. In addition to steady-state measurements, a number of ultrafast spectroscopic studies [109-112] have been performed on PNA to understand the dynamics of excited states after photoexcitation. It is well known from these studies that the S<sub>1</sub> state of PNA exhibits a CT character with a large dipole moment of ~15 D and relaxes very rapidly (< 0.3 ps) to the S<sub>0</sub> state via internal conversion (IC) or by intersystem crossing (ISC) to the triplet manifold. Participation of vibrational degrees of freedom during and after IC has been studied using transient absorption and vibrational spectroscopies.

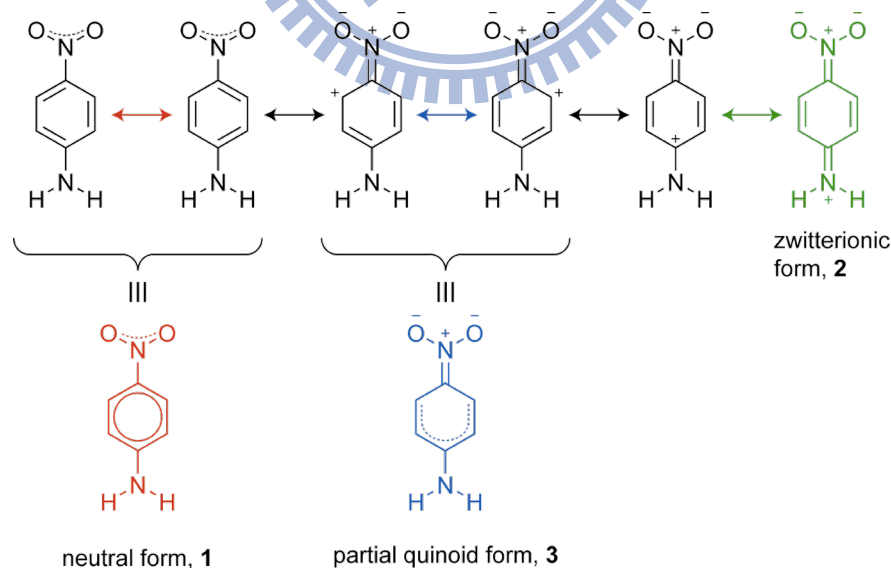


**Figure IV–1.** Representative resonance structures of PNA and their hybrids: neutral form (1), zwitterionic form (2), and partial quinoid form (3).

Conventionally, using a two-state valence-bond model, the electronic states of PNA are expressed as a hybrid of the two basis states **1** and **2** as shown in Figure IV–1. More specifically, the ground state is predominantly the neutral form **1**, whereas the  $S_1$  state has a considerable contribution of the zwitterionic form **2**, giving rise to a large change in dipole moment from  $\sim 6$  D in the  $S_0$  state to  $\sim 15$  D in the  $S_1$  state [108]. Because the  $T_1$  state is a primary channel for the photophysical and photochemical processes in the ns– $\mu$ s time region, it is desirable to obtain detailed molecular information on this state. Schuddeboom et al. [111] used time-resolved microwave conductivity to determine the lifetime and dipole moment of the  $T_1$  state in benzene and dioxane. It is shown that the dipole moment of  $T_1$  PNA takes on values in the range of 9–11 D depending on the solvent. Thomsen and co-workers [112] measured the transient absorption spectrum in the 340–960 nm range, of PNA excited at 400 nm, which was assigned to vibrationally hot PNA molecules in the ground state and triplet–triplet absorption bands. A recent theoretical investigation by Kosenkov and Slipchenko [106] predicted that the  $T_1$  state ( $1^3A_1$ ) has a much smaller dipole moment (8.7 D) than the CT  $S_1$  state (12.9 D). Although it would be reasonable to account for these observations in the framework of the two-state model assuming that the  $T_1$  state of PNA has a CT structure [113] analogous to the  $S_1$  state, this analogy needs to be critically tested by obtaining more direct information on the bonding structure of PNA in the  $T_1$  state. Vibrational spectroscopy is undoubtedly a powerful approach that permits one to access such information. In the present work, we aim to provide new insights into the electronic and molecular structure of  $T_1$  PNA on the basis of experimental and theoretical IR spectra.

## IV-2 Materials and Methods

In this section, sample preparation methods, experimental conditions and computational techniques that were used to characterize the  $T_1$  PNA are described briefly.

### IV-2.1 Sample Preparation Methods

All chemicals were purchased from Sigma Aldrich unless otherwise indicated. PNA (>99%) was purified by recrystallization from benzene (Alfa Aesar) before use. Two  $^{15}\text{N}$ -substituted isotopomers of PNA were synthesized according to published methods. *p*-( $^{15}\text{N}$ )Nitroaniline (PNA- $^{15}\text{NO}_2$ ) was synthesized by the nitration of acetanilide (97%) with  $\text{K}^{15}\text{NO}_3$  (98 atom %  $^{15}\text{N}$ ) and subsequent hydrolysis. The product was recrystallized from ethanol. *p*-

Nitro(<sup>15</sup>N)aniline (PNA-<sup>15</sup>NH<sub>2</sub>) was obtained by nitrating acetanilide-<sup>15</sup>N (98 atom % <sup>15</sup>N) with reagent-grade KNO<sub>3</sub> (>99%), followed by hydrolysis. The product was separated by column chromatography on silica gel using first *n*-hexane and then *n*-hexane/ethyl acetate (80:20 v/v) as eluents. The synthesized isotopomers were characterized by <sup>1</sup>H-NMR, EI mass, UV-visible and FT-IR spectroscopies. <sup>1</sup>H-NMR (300 MHz, DMSO-*d*<sub>6</sub>): δ = 7.94–7.91 (m, 2H), 6.7 (s, 2H), 6.59–6.56 (m, 2H); EIMS *m/z*: M<sup>+</sup> 139. For UV/Vis and FTIR measurements, CD<sub>3</sub>CN (99.8 atom % D, Cambridge Isotope Laboratories) was used as solvent. The UV/Vis spectra of PNA-<sup>15</sup>NH<sub>2</sub> and PNA-<sup>15</sup>NO<sub>2</sub> evidenced no noticeable difference from that of normal PNA. The IR spectra of the compounds are of primary interest in this work, so we will discuss them in detail in Section IV-3.4.

#### IV-2.2 Nanosecond Time-Resolved Infrared Spectroscopy

The details of the nanosecond time-resolved IR spectrometer have been described in Chapter II. In the present study the third harmonic of the Q-switched Nd:YAG laser (355 nm; ~7 ns duration; 56 μJ energy; 500 Hz repetition rate) was used to photoexcite PNA. The excitation wavelength lies very close to the absorption maximum (364 nm) of PNA in CD<sub>3</sub>CN (shown in Figure IV–2), which corresponds to the S<sub>1</sub> ← S<sub>0</sub> transition.

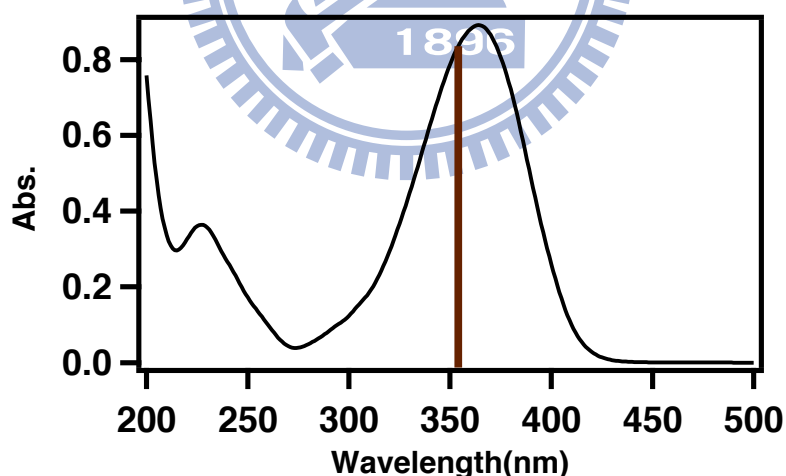


**Figure IV–2.** UV-Vis Spectrum of PNA (500 μM) in CD<sub>3</sub>CN. Brown line represents the laser excitation wavelength (355 nm) chosen for pumping PNA to the S<sub>1</sub> state.

The changes in absorption spectrum upon photoexcitation were probed with MIR light derived from a ceramic IR emitter. The probe light transmitted through the sample of 100 μm thick. TRIR measurements were performed in the fingerprint region (1200–1700 cm<sup>-1</sup>, where IR bands of CD<sub>3</sub>CN have no interference with the transient IR spectrum. A spectral resolution

of  $8\text{ cm}^{-1}$  was used. The concentration of PNA in  $\text{CD}_3\text{CN}$  was kept as low as  $0.25\text{ mM}$  such that the depletion of the ground-state absorption almost fully recovers at longer delay times and no long-lived photoproducts of PNA were detected to a measurable extent (see Section IV-3.1). In a normal run, the sample solution in the reservoir was continuously bubbled with argon gas, whereas in the oxygen quenching experiment, it was saturated with oxygen gas. The  $S_0$  state IR spectra of PNA and its isotopomers were also recorded on a JASCO FT/IR-6100 spectrometer with a spectral resolution of  $2\text{ cm}^{-1}$ . All measurements were performed at room temperature.

### IV-2.3 Computational Details

DFT calculations were performed with the B3LYP functional and the cc-pVTZ basis set as implemented in Gaussian 09 [72]. Geometry optimization was done with tight convergence criteria, followed by frequency calculations with IR intensity determination. Polarizable continuum model (PCM) calculations were also tested to see the implicit effects of solvent molecules on the solute. Calculated IR spectra were plotted with a Gaussian spectral envelope with a FWHM of  $16\text{ cm}^{-1}$ . In the engineered spectra (see Section IV-3.5 for details), we slightly elongated the C–NH<sub>2</sub> distance and performed partial geometry optimization (with the C–NH<sub>2</sub> distance frozen) followed by frequency determination for such a non-equilibrium structure; all vibrational modes are non-imaginary and, in fact, differ only slightly (up to  $15\text{ cm}^{-1}$ ) from the original spectrum. All calculated vibrational frequencies discussed in this paper were scaled by a constant factor of 0.972. All computational work was done by Mr. Shu-Wei Chang and Prof. Henryk A. Witek.

## IV-3 Results and Discussion

### IV-3.1 Nanosecond TRIR Spectra of PNA in $\text{CD}_3\text{CN}$ under Ar Environment

In this section, results of the TRIR measurements of PNA in  $\text{CD}_3\text{CN}$  with Ar bubbling are discussed in detail. TRIR spectra of PNA along with its  $S_0$  spectrum are shown in Figure IV-3. The FTIR spectrum of  $S_0$  PNA displays four vibrational bands at  $1316$ ,  $1503$ ,  $1600$  and  $1635\text{ cm}^{-1}$ . These peak positions correspond well with the spectra reported in the literature [35,96,105]. A shoulder at  $\sim 1330\text{ cm}^{-1}$  accompanies the  $1316\text{ cm}^{-1}$  band. Based on the results of the DFT calculations performed on  $S_0$  PNA (see below), these four bands are assigned to symmetric and anti-symmetric  $\text{NO}_2$  stretching modes, admixtures of the  $\text{NH}_2$  scissors and the

C–C stretch, respectively. The vibrational assignments agree well with the literature [35,96,105].

The transient MIR spectrum (Figure IV–3b) displays three positive bands with peak positions at 1250, 1480, and 1605  $\text{cm}^{-1}$  and four negative bands whose peak positions coincide exactly with the peak positions in the  $S_0$  spectrum shown in Figure IV–3a. The negative bands in the difference spectrum are due to the decrease of the ground state population usually termed photobleach, whereas the positive bands are due to the generation of the transient species after photoexcitation.

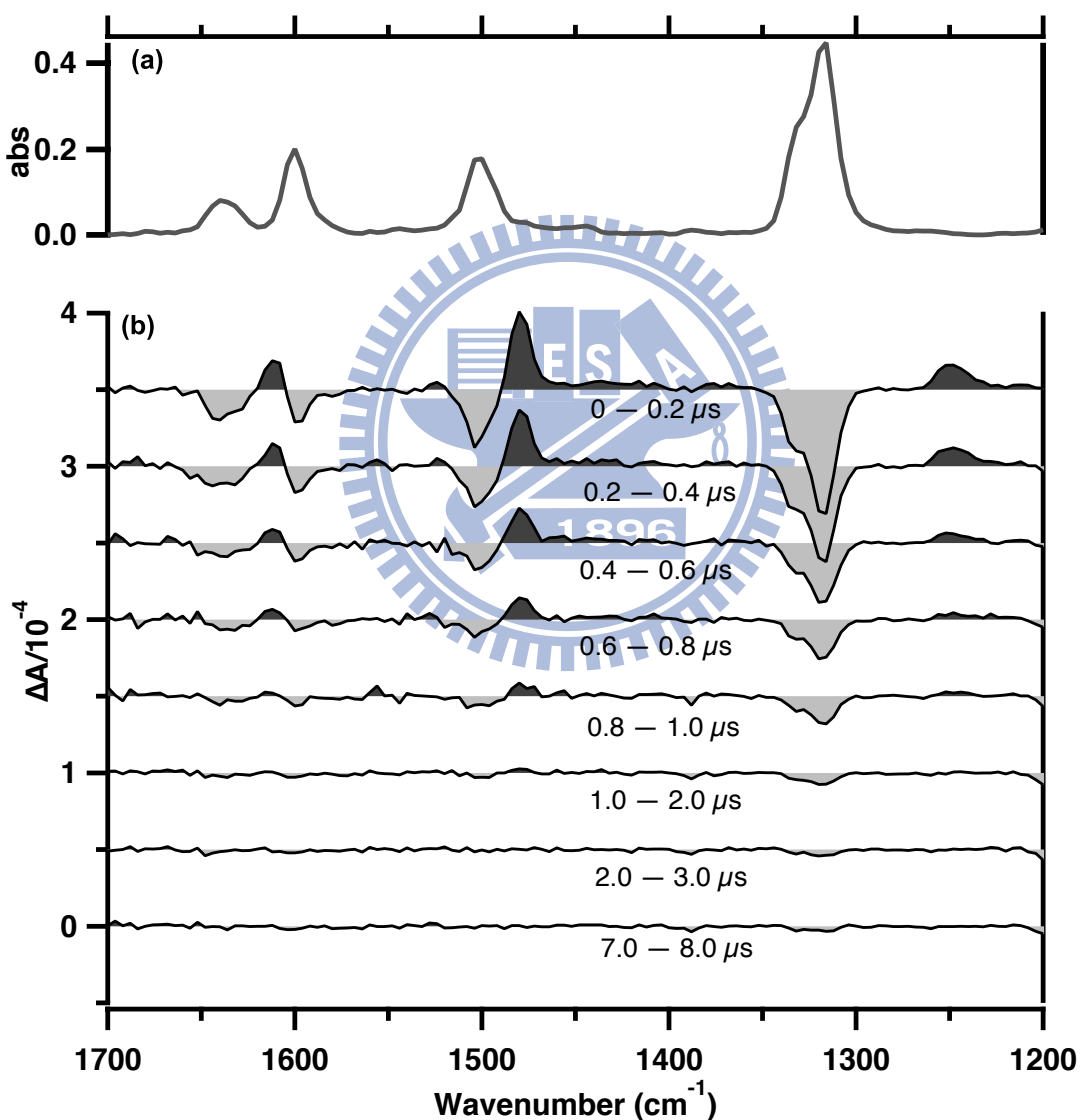


**Figure IV–3.** Ground-state ( $S_0$ ) spectrum (a) and time-resolved IR difference spectra (b) of PNA in  $\text{CD}_3\text{CN}$  (0.25 mM), excited at 355 nm with Ar bubbling. Each time-resolved spectrum is offset by  $5 \times 10^{-5}$  for clarity.

All the transient bands shown in Figure IV–3b rise instantaneously after photoexcitation and decay synchronously within 1  $\mu\text{s}$  along with the recovery of the ground state. There is only little bleach remaining after 8  $\mu\text{s}$ . As discussed earlier, the lifetime of the  $S_1$  state is very short and it relaxes to the  $S_0$  state very rapidly via IC and to the  $T_1$  state via ISC. The time constants for IC and ISC in water are, respectively, 250 fs [110] and 10 ps [112], according to earlier transient absorption studies [110-112]. The dynamics of the  $S_1$  state is too fast to be observed by our TRIR apparatus. Thus, the transient species observed in Figure IV–3b must be the  $T_1$  state of PNA. From the earlier studies, the quantum yield of ISC is  $\Phi_{\text{ISC}} \approx 0.4$  in dioxane ( $\epsilon = 2.25$ ) and  $\Phi_{\text{ISC}} \approx 0.03$  in water ( $\epsilon = 80$ ) [112]. The dielectric constant of  $\text{CD}_3\text{CN}$  ( $\epsilon = 37.5$ ) lies between those of dioxane and water, so  $\Phi_{\text{ISC}}$  between 0.4 and 0.03 is expected for PNA in  $\text{CD}_3\text{CN}$ .

### IV-3.2 SVD analysis of the TRIR Spectra of PNA in $\text{CD}_3\text{CN}$

In this section, results of the SVD analysis [23,38,114] we performed on the TRIR data (represented by a  $125 \times 1000$  matrix) are shown in order to obtain the information of both structurally and dynamically distinct transient species of PNA. Singular values yielded by the SVD of the TRIR data matrix are plotted in Figure IV–4a. The spectral and temporal profiles of the largest three singular values are shown in Figure IV–4b and c, respectively. Inspection of the spectral components and temporal profiles shows that the analyzed matrix has only one significant component. It is worthy to note that though the second and third singular values are not smaller by an order of magnitude than the largest singular value, they do not exhibit any physically meaningful spectral and temporal profiles. They are most likely due to noises.

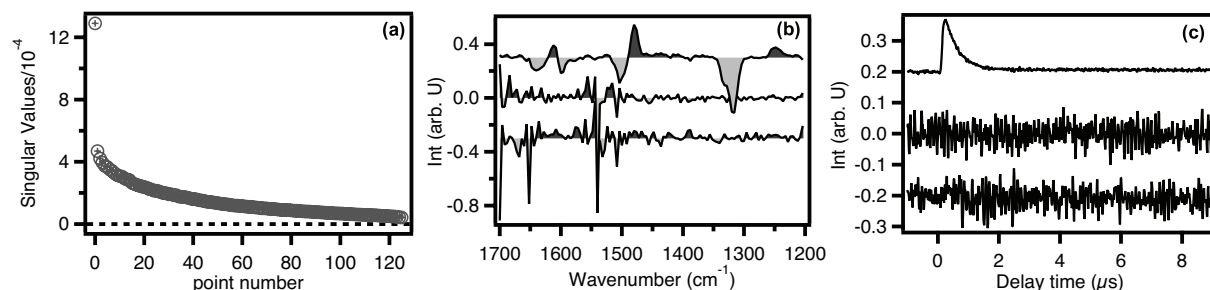


**Figure IV–4.** (a) Plot of singular values obtained from the SVD of the TRIR data matrix. (b,c) Spectral (b) and temporal (c) components corresponding to the largest three singular values. Each spectral and temporal component is offset by 0.3 and 0.2 respectively, for clarity.

The transient IR spectrum and time profile of the first SVD component are shown in Figure IV–5. The spectrum shown in Figure IV–5a resembles the time-resolved spectra measured between 0–200 ns shown in Figure IV–3b, and the temporal profile shown in Figure IV–5b represents the overall dynamics of the transient species. A curve fitting analysis using an exponential function convolved with a Gaussian instrumental response function (IRF) is performed on the temporal profile shown in Figure IV–5b. A time constant of 430 ns is obtained from the fit, which is consistent with the reported time constant for the  $T_1$  state of PNA (434 ns in ACN [103] and 250 ns in dioxane [111]).

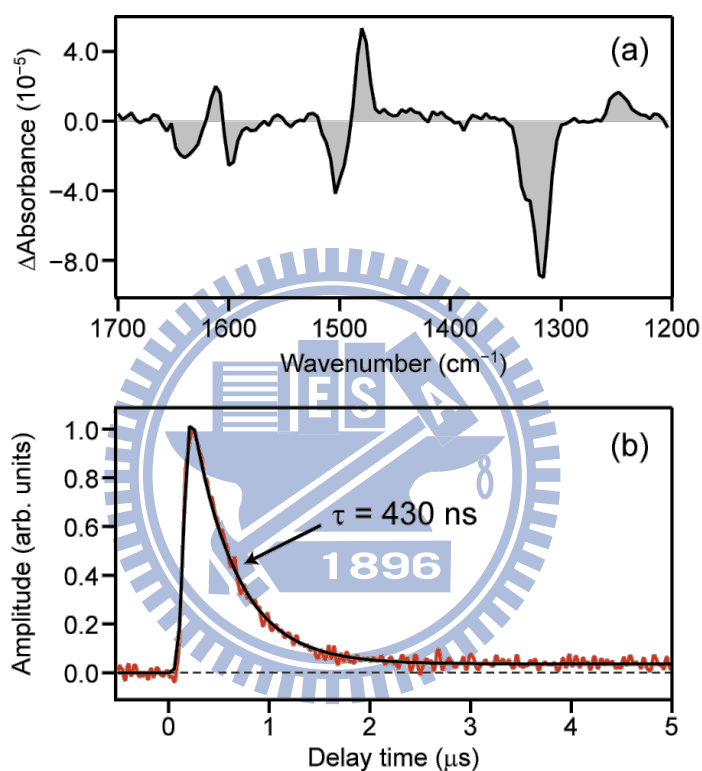


**Figure IV–5.** Results of a SVD analysis of the time-resolved IR difference spectra of PNA in  $\text{CD}_3\text{CN}$  with Ar bubbling. (a) Decomposed spectral component. (b) Decomposed temporal component (red line) and the best fit (black line) to an exponential function convolved with a Gaussian IRF. The exponential time constant is determined to be  $\tau = 430 \text{ ns}$ .

### IV-3.3 TRIR Spectra of PNA in $\text{CD}_3\text{CN}$ under $\text{O}_2$ Environment

In this section, the TRIR spectroscopic measurements of PNA measured in  $\text{CD}_3\text{CN}$  with  $\text{O}_2$  bubbling are discussed. The measurements should provide additional evidence for the assignments of the transient species to the  $T_1$  state. The results are shown in Figure IV–6. The



TRIR spectra shown in Figure IV–6a resemble in pattern with the transients seen in Figure IV–3b, but the transient bands decay much faster compared to the experiment with Ar bubbling, indicating efficient quenching by molecular O<sub>2</sub>.

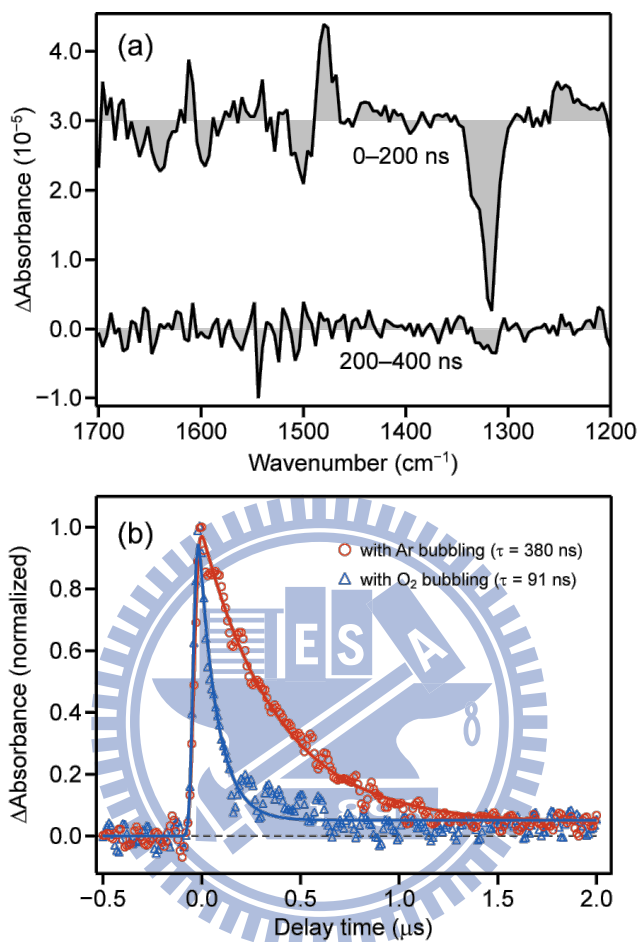


**Figure IV–6.** (a) Time-resolved IR difference spectra of PNA in CD<sub>3</sub>CN with O<sub>2</sub> bubbling: 0–200 ns and 200–400 ns after photoexcitation. (b) Kinetic profiles of the transient band at 1248 cm<sup>-1</sup> with Ar bubbling (red circle) and with O<sub>2</sub> bubbling (blue triangle). The time profiles have been normalized to the same maximum height. Solid lines are the best fits to an exponential convolved with a Gaussian IRF.

The kinetic profiles of the 1248 cm<sup>-1</sup> transient band measured under Ar and O<sub>2</sub> bubbling conditions (Figure IV–6b) show clear evidence of the O<sub>2</sub> quenching effect. A curve fitting analysis determines an exponential time constant of 380 (±11) ns with Ar bubbling, which is reduced to 91 (±5) ns with O<sub>2</sub> bubbling. The uncertainties quoted here represent standard deviations of three independent measurements. The results further confirm that the observed transients in the TRIR difference spectra are assigned to T<sub>1</sub> PNA.

#### IV-3.4 Experimental IR Spectra of the T<sub>1</sub> State of PNA and Its Isotopomers

In this section, the MIR spectrum of T<sub>1</sub> PNA and its isotopomers are compared and the effects of isotope substitution (<sup>15</sup>N substitution in the NO<sub>2</sub> and the NH<sub>2</sub> groups of PNA) on the IR spectra of S<sub>0</sub> and T<sub>1</sub> PNA are discussed. The triplet IR spectra of PNA, PNA-<sup>15</sup>NO<sub>2</sub>, and PNA-<sup>15</sup>NH<sub>2</sub> can be calculated by adding the appropriately scaled spectrum of the S<sub>0</sub> state in such a way that all the negative bands associated with the S<sub>0</sub> state of PNA are compensated [23], [32]. The resulting IR spectra of the three PNA isotopomers in the T<sub>1</sub> state are shown in Figure IV-7 along with their S<sub>0</sub> FTIR spectra. The IR spectrum of T<sub>1</sub> PNA (Figure IV-7d) has a very weak band at 1320 cm<sup>-1</sup>. This band cannot be regarded as a subtraction artifact because the scaling factor we used could successfully compensate all the vibrational bands corresponding to the S<sub>0</sub> state. The experimental vibrational frequencies for the S<sub>0</sub> and T<sub>1</sub> states determined for all the three compounds are listed in Table IV-1. From Figure IV-7, it is clear that the <sup>15</sup>N substitution in the NH<sub>2</sub> group of PNA does not affect the spectra of the S<sub>0</sub> and T<sub>1</sub> states of PNA (compare Figure IV-7a and b for S<sub>0</sub> and Figure IV-7d and e for T<sub>1</sub>), whereas the <sup>15</sup>N substitution in the NO<sub>2</sub> group of PNA does affect the spectra of the S<sub>0</sub> and T<sub>1</sub> states of PNA (compare Figure IV-7a and c for S<sub>0</sub> and Figure IV-7d and f for T<sub>1</sub>). The region between 1420–1520 cm<sup>-1</sup> and a doublet feature at ~1320 cm<sup>-1</sup> are affected for the S<sub>0</sub> state (see Figure IV-7c) and the vibrational band at 1250 cm<sup>-1</sup> is shifted by ~25 cm<sup>-1</sup> for the T<sub>1</sub> state (see Figure IV-7f) as a result of the <sup>15</sup>N substitution in the NO<sub>2</sub> group of PNA.

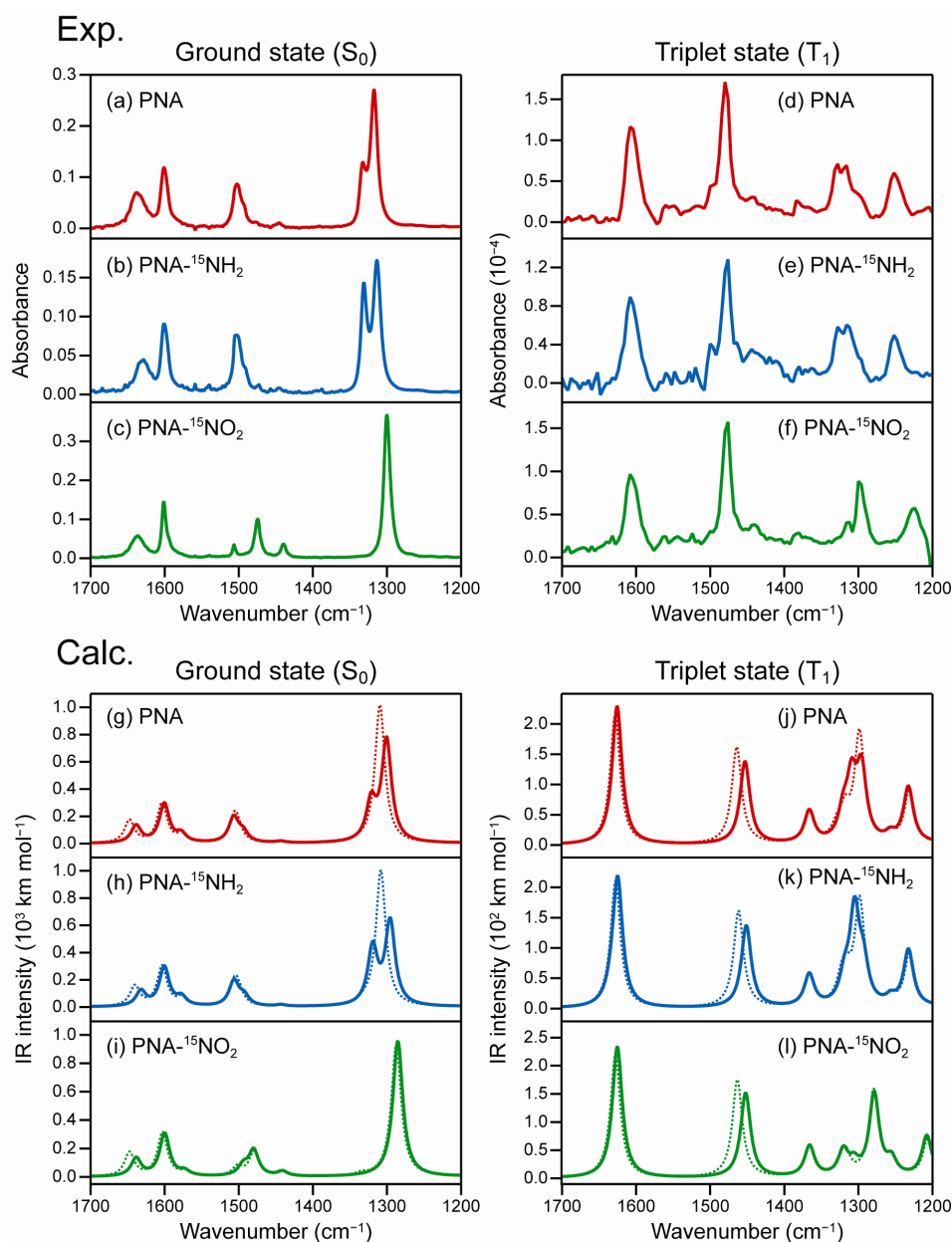


**Figure IV–7.** Upper panels: experimental IR spectra of PNA (red line) and its isotopomers, PNA-<sup>15</sup>NH<sub>2</sub> (blue) and PNA-<sup>15</sup>NO<sub>2</sub> (green). (a–c) Ground-state (S<sub>0</sub>) spectra recorded with an FT-IR spectrometer. (d–f) Lowest excited triplet-state (T<sub>1</sub>) spectra obtained by compensating the depletion of the ground-state absorption. Lower panels: calculated IR spectra of PNA (red line), PNA-<sup>15</sup>NH<sub>2</sub> (blue), and PNA-<sup>15</sup>NO<sub>2</sub> (green), using the PNA+2ACN model with (solid line) and without (dotted line) elongation of the C–NH<sub>2</sub> bond by 0.012 Å. (g–i) The ground state. (j–l) The T<sub>1</sub> state. See text for details.

**Table IV–1.** Experimental and Calculated Vibrational Frequencies and Assignments of Major IR Bands (in 1200–1700  $\text{cm}^{-1}$ ) of PNA, PNA- $^{15}\text{NH}_2$ , and PNA- $^{15}\text{NO}_2$  in the Ground State and the Lowest Excited Triplet State.

Experiment <sup>a</sup>			DFT calculation <sup>b</sup>			Assignment <sup>c</sup>
PNA	PNA- $^{15}\text{NH}_2$	PNA- $^{15}\text{NO}_2$	PNA	PNA- $^{15}\text{NH}_2$	PNA- $^{15}\text{NO}_2$	(approximate description)
Ground ( $S_0$ ) state						
1636	1630	1637	1638	1632	1638	$\delta_s(\text{NH}_2 \text{ sci.})$
1600	1600	1601	1600	1600	1600	$\nu(\text{C-C}), \delta_s(\text{NH}_2 \text{ sci.})$
			1578	1577	1573	$\nu(\text{C-C}), \nu_{\text{as}}(\text{NO}_2), \rho(\text{NH}_2)$
1503	1503	1475	1507	1506	1480	$\nu_{\text{as}}(\text{NO}_2), \nu(\text{C-C})$
1494	1494	1506	1494	1492	1494	$\delta(\text{C-H}), \nu(\text{C-C}), \nu(\text{C-NH}_2),$ $\delta_s(\text{NH}_2 \text{ sci.})$
		1475				
1332	1331		1321	1319	1313	$\nu_s(\text{NO}_2), \delta(\text{C-H}),$ op. $\nu(\text{C-NH}_2)$ and $\nu(\text{C-NO}_2)$
1317	1314	1300	1300	1296	1285	$\nu_s(\text{NO}_2), \delta(\text{C-H}),$ ip. $\nu(\text{C-NH}_2)$ and $\nu(\text{C-NO}_2)$
Triplet ( $T_1$ ) state						
1605	1606	1605	1626	1624	1625	$\delta_s(\text{NH}_2 \text{ sci.}), \nu(\text{C-C})$
1480	1476	1478	1453	1451	1452	$\delta(\text{C-H}), \nu(\text{C-C}), \nu(\text{C-NH}_2),$ $\delta_s(\text{NH}_2 \text{ sci.})$
			1366	1366	1366	$\nu(\text{C-C}), \rho(\text{NH}_2)$
			1320	1319	1320	
~1320	~1320	~1300	1309	1305	1306	$\nu_s(\text{NO}_2), \delta(\text{C-H}),$ ip. $\nu(\text{C-NH}_2)$ and $\nu(\text{C-NO}_2)$
			1296	1293	1279	$\nu_s(\text{NO}_2), \delta(\text{C-H}),$ op. $\nu(\text{C-NH}_2)$ and $\nu(\text{C-NO}_2)$
			1257	1256	1255	
1250	1250	1225	1232	1232	1207	$\nu_{\text{as}}(\text{NO}_2), \nu(\text{C-C}), \rho(\text{NH}_2)$

<sup>a</sup>Taken from FT-IR spectra.

<sup>b</sup>PNA+2ACN/B3LYP with elongation of the C–NH<sub>2</sub> distance by 0.012 Å. Scaling factor = 0.972.

<sup>c</sup> $\nu$ , stretching;  $\delta$ , in-plane bending;  $\rho$ , rocking; sci., scissoring; op., out of phase combination; ip., in-phase combination.

### IV-3.5 Calculated IR spectra of the T<sub>1</sub> State of PNA and Its Isotopomers

In this section, theoretical interpretation for the experimental IR spectra of PNA and its isotopomers in CD<sub>3</sub>CN is presented. In general, for modeling an IR spectrum in solution phase, we have to perform time-dependent investigation of the dynamics of an ensemble of PNA and ACN at a finite temperature. Such a study involves running a molecular dynamics trajectory for an ensemble and obtain the IR spectrum via the Fourier transform of the recorded dipole moment autocorrelation function. Unfortunately such a study is not practically feasible particularly for excited states at the present level of development of computational methods. Instead we used DFT with B3LYP exchange correlational function for geometry optimization of the molecule, followed by determination of the IR spectrum in a double harmonic approximation, in which both positions and intensities of the bands are determined by retaining only the lowest non-vanishing terms in the Taylor expansions of the potential energy and dipole moment. The lack of anharmonicity in the calculated B3LYP spectra is partially compensated by performing a uniform scaling of the computed frequencies by a factor of 0.972.

For modeling IR spectra of molecules in the condensed phase, the choice of an appropriate molecular model is very important. Bare molecules in the gas phase are often used with the assumption that there is no essential difference between molecules in the gas and condensed phases. In order to test this supposition, we first simulate the IR spectrum of S<sub>0</sub> PNA, whose experimental IR spectrum is recorded precisely. Once we find a suitable molecular model to reproduce the IR spectrum of S<sub>0</sub> PNA in a satisfactory manner in terms of both peak positions and intensities, we then apply that model to determine the IR spectrum of T<sub>1</sub> PNA.

As shown in Figure IV-3a, the S<sub>0</sub> state spectrum of PNA has four principle bands at 1320, 1500, 1600, and 1635 cm<sup>-1</sup>. Among these four vibrational bands, the NO<sub>2</sub> symmetric stretch band at 1320 cm<sup>-1</sup> is the most characteristic and this band has a hump at 1300 cm<sup>-1</sup>. The DFT/B3LYP calculated IR spectrum of gas-phase PNA contrasts with the experimental spectrum, as can be seen from Figure IV-8b. The NO<sub>2</sub> symmetric stretch in the calculated spectrum shows a reversed intensity pattern between the higher and lower wavenumber peaks compared to the experimental spectrum with a clearer separation of the two peaks. The region between 1450–1650 cm<sup>-1</sup> also shows a prominent difference. These results show that the solvation of PNA by CD<sub>3</sub>CN has substantial influence on IR spectrum and that the gas-phase model cannot be used to interpret the IR spectrum of PNA even in the S<sub>0</sub> state.

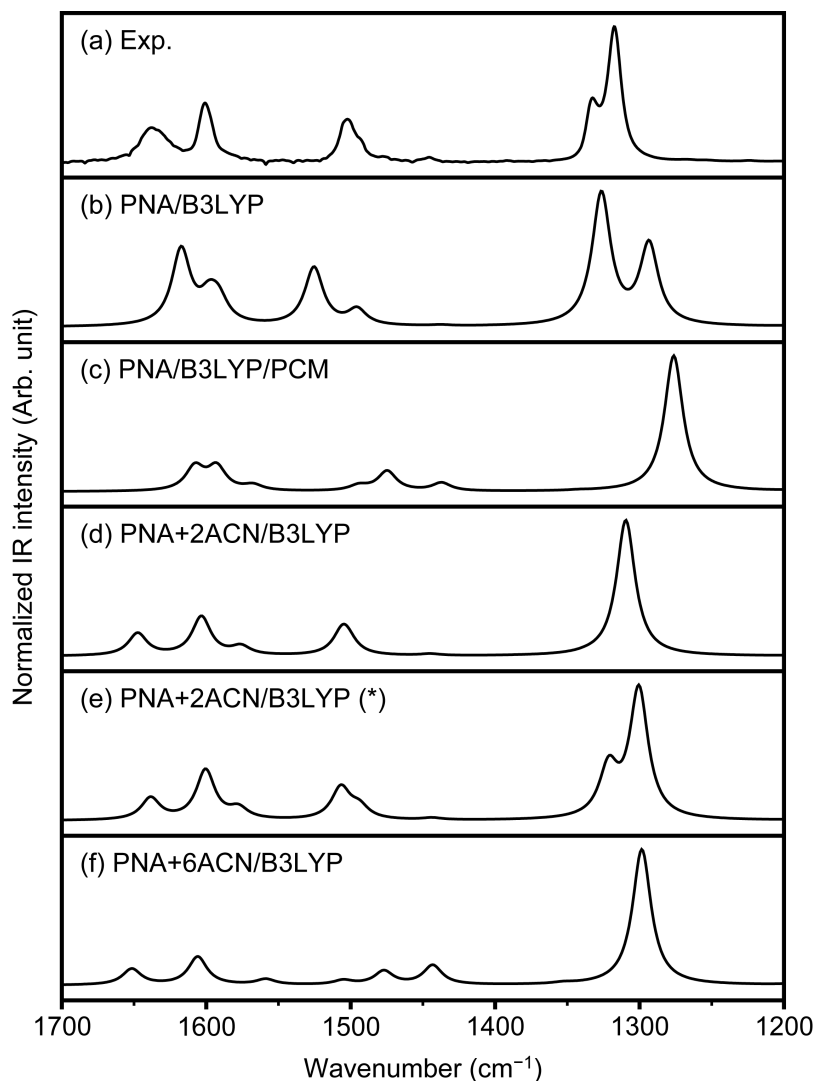


**Figure IV–8.** Comparison of experimental and theoretical DFT/B3LYP IR spectra of PNA in the ground state. (a) FT-IR spectrum of PNA in CD<sub>3</sub>CN (0.25 mM), (b) a gas-phase molecular model, (c) the PCM model, (d) an explicitly solvated model with two CD<sub>3</sub>CN molecules attached to the NH<sub>2</sub> group (the PNA+2ACN model), (e) the PNA+2ACN model with elongation of the C–NH<sub>2</sub> bond by 0.012 Å, and (f) an explicitly solvated model with six CD<sub>3</sub>CN molecules.

It is customary to use an implicit solvation model to account for the solvent effects in which the solvent is considered as a continuum with a specified dielectric constant ( $\epsilon = 37.5$  for CD<sub>3</sub>CN). A combination of DFT/B3LYP with the polarizable continuum model (PCM) has been employed to simulate the IR spectrum of S<sub>0</sub> PNA. However, this model did not bring any desired effect to the IR spectrum of PNA, as can be seen from Figure IV–8c. The doublet feature at 1320 cm<sup>-1</sup> and the 1635 cm<sup>-1</sup> band are missing. The 1600 cm<sup>-1</sup> band shows a

doublet feature and the region between 1400–1500  $\text{cm}^{-1}$  also shows a marked difference from experiment.

As the gas-phase and PCM calculations have failed to simulate the experimental IR spectrum of PNA in a reasonable manner, we turned to explicit solvation models that involve attachment of one to six  $\text{CD}_3\text{CN}$  molecules either to the  $\text{NO}_2$  and  $\text{NH}_2$  group, or aligned along a ring. A Raman study on the dependence on mole fraction of ACN in  $\text{ACN}/\text{CCl}_4$  binary mixtures [97] and an IR electroabsorption work on PNA in  $\text{ACN}/\text{CCl}_4$  [102] suggest that an explicit solvation model in which  $\text{CD}_3\text{CN}$  is attached to PNA via hydrogen bonding explains their experiment results well. Fortunately, an explicit solvation model with two  $\text{CD}_3\text{CN}$  molecules attached to the  $\text{NH}_2$  group (denoted PNA+2ACN) is found to reproduce the overall IR spectrum of PNA except for the hump of the 1320  $\text{cm}^{-1}$  band (see Figure IV–8d). Having six  $\text{CD}_3\text{CN}$  molecules in solvation (denoted PNA+6ACN) results in poorer agreement with experiment in the 1400–1500  $\text{cm}^{-1}$  region.

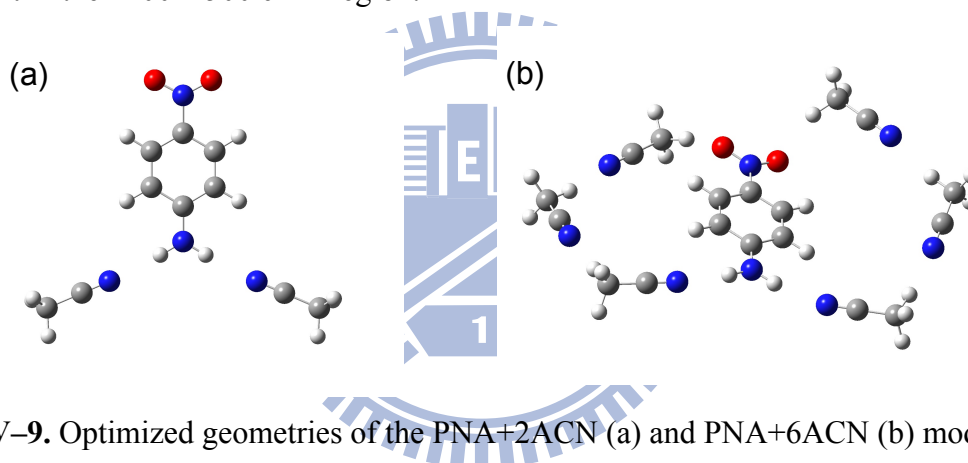


**Figure IV–9.** Optimized geometries of the PNA+2ACN (a) and PNA+6ACN (b) models.

The optimized geometries in the PNA+2ACN and PNA+6ACN models are shown in Figure IV–9. As a matter of fact, one to three  $\text{CD}_3\text{CN}$  molecules could reproduce the spectral pattern as nicely as the PNA+2ACN model except for the changes in relative band intensities. It is intuitive to think that in PNA, only the  $\text{NH}_2$  group can participate in H-bonding. However, the DFT calculation results predict that the binding energy of  $\text{CD}_3\text{CN}$  to the  $\text{NH}_2$  and  $\text{NO}_2$  groups is of similar order of magnitude: 5.5 and 3.5 kcal/mol, respectively.

The optimized structures of PNA with the explicit solvation models show a slight deviation from the equilibrium geometry, which concerns in the out-of-plane angles of the  $\text{NH}_2$  and  $\text{NO}_2$  groups and the  $\text{C-NH}_2$  and  $\text{C-NO}_2$  distances. We have anticipated that the out-of-plane, low-frequency motions of the  $\text{NH}_2$  and  $\text{NO}_2$  groups may have substantial influence on the simulated IR spectra [109]. It has turned out that this effect is negligible [87,99], but in the course of this investigation, we have found that some part of the spectrum changes

drastically with the variation of the C–NH<sub>2</sub> distance. A slight elongation of the C–NH<sub>2</sub> bond length (by 0.012 Å) from its equilibrium bond length (1.352 Å) produces a small hump at the 1300 cm<sup>-1</sup> band. This slight elongation has brought perfect agreement between the simulated and experimental IR spectra of S<sub>0</sub> PNA, which can be seen from Figure IV–7a and g and Figure IV–8a and e). The origin of the doublet feature at ~1320 cm<sup>-1</sup> is a subject of debate [35,96-98,100,102]. Two possible mechanisms have been proposed to account for the small hump of the 1320 cm<sup>-1</sup> band. One of them is Fermi resonance [35,96], and the other one is the existence of two different solvated forms of PNA [97,102]. However, according to our DFT calculations results, the higher and lower wavenumber components of the doublet are found to arise from the NO<sub>2</sub> symmetric stretch coupled with out-of-phase and in-phase combinations of the C–NH<sub>2</sub> and C–NO<sub>2</sub> stretches, respectively (see Table IV–1). We also find that the relative IR intensities are profoundly affected by the geometry of PNA as well as explicit solvation.

The slight elongation of C–NH<sub>2</sub> distance by 0.012 Å is justified as follows. First, the typical error in the estimation of equilibrium bond lengths in DFT calculations is 0.01 Å. Second, the C–NH<sub>2</sub> bond length used to reproduce the experimental spectrum (1.364 Å) lies between the equilibrium bond length of bare gas-phase PNA (1.343 Å) and solvated PNA molecule (1.375 Å). Finally, such a small elongation might have an effect on the intensity redistribution but it should not alter the positions of vibrational bands. Re-optimization of the geometry of PNA keeping the C–NH<sub>2</sub> distance frozen and subsequent re-calculation of the IR spectrum yield a frequency change of at most 15 cm<sup>-1</sup>.

A physical interpretation of the slight elongation of the C–NH<sub>2</sub> distance can be obtained by taking into account the differences between the intrinsic static nature of the models used in quantum chemical calculations and the dynamic nature of the actual vibrating molecule. Quantum chemical calculations usually give us the information about the (static) equilibrium bond distances ( $r_e$ ), but it would be more desirable to consider the distances averaged over the ground vibrational wave functions ( $r_0$ ), which provide more physically meaningful information about the time-averaged interatomic distances in a molecule. For a purely harmonic vibration, these two quantities would be equal. However, the C–NH<sub>2</sub> bond stretch, as nearly any stretching vibration, possesses an anharmonic vibrational potential, for which  $r_0$  is usually slightly larger than  $r_e$ . Additional support for the C–NH<sub>2</sub> bond elongation comes from the simulated IR spectra of PNA-<sup>15</sup>NH<sub>2</sub> and PNA-<sup>15</sup>NO<sub>2</sub>. In experiment (upper left panel of Figure IV–7), the <sup>15</sup>N substitution in the NH<sub>2</sub> group leads to a larger splitting between the doublet components at ~1320 cm<sup>-1</sup>, whereas the <sup>15</sup>N substitution in the NO<sub>2</sub> group removes



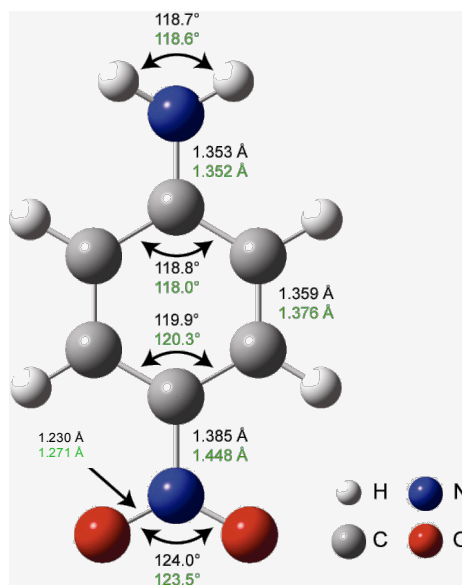
the doublet character of the  $1320\text{ cm}^{-1}$  and splits the  $1500\text{ cm}^{-1}$  band into three bands. The PNA+2ACN model (dotted line, lower left panel of Figure IV-7) predicts correctly the isotope substitution effects in the  $\text{NO}_2$  group but fails to predict the distinct doublet structure of the  $1320\text{ cm}^{-1}$  band. In contrast, the PNA+2ACN model with slightly elongated C-NH<sub>2</sub> bond (solid line, lower left panel of Figure IV-7) predicts correctly the isotope substitution effects in both NH<sub>2</sub> and NO<sub>2</sub> groups.

We have demonstrated above that the PNA+2ACN model with slightly elongated C-NH<sub>2</sub> bond is capable of reproducing all the accumulated spectral evidence for the S<sub>0</sub> state of PNA. We are therefore ready to interpret the IR spectrum of the T<sub>1</sub> PNA shown in Figure IV-7d. The experiment detects four principal bands in the IR spectrum of T<sub>1</sub> PNA, located approximately at 1250, 1320, 1480, and 1605  $\text{cm}^{-1}$ . The engineered PNA+2ACN model (Figure IV-7j) closely resembles this experimental spectrum, reproducing these bands at 1232, 1300, 1453 and 1626  $\text{cm}^{-1}$ , respectively. The assignments of these bands are as follows. The band at 1232  $\text{cm}^{-1}$  corresponds predominantly to the NO<sub>2</sub> antisymmetric stretch. The intense composite band at  $\sim 1300\text{ cm}^{-1}$  has a complicated vibrational composition, namely, a mixture of in-plane C-H bending, C-NH<sub>2</sub> and C-NO<sub>2</sub> stretches, C-C stretch, and NO<sub>2</sub> symmetric stretch. The band at 1453  $\text{cm}^{-1}$  is a mixture of in-plane C-H bending and the C-NH<sub>2</sub> and C-NO<sub>2</sub> stretches. The band at 1626  $\text{cm}^{-1}$  originates from a mixture of the NH<sub>2</sub> scissoring motion and C-C stretch; the analogous band appears in the IR spectrum of the ground state at 1635  $\text{cm}^{-1}$ , although much less intense. In addition to these four bands, the simulated IR spectrum has a low-intensity band at 1366  $\text{cm}^{-1}$ , which originates from in-plane C-H bending. A close inspection of Figure IV-7d shows a small hump located at nearly the same position as this band; however, the inaccuracies present in the compensated spectrum prevent us from being fully conclusive on the 1366  $\text{cm}^{-1}$  band. As can be seen from Figure IV-7d-f and Figure IV-7j-l, the PNA+2ACN model with slightly elongated C-NH<sub>2</sub> bond again does an excellent job of reproducing the experimental IR spectra of all the three isotopomers in the T<sub>1</sub> state. The vibrational frequencies and assignments for T<sub>1</sub> PNA derived from the calculations are summarized in Table IV-1.

#### IV-4 Structural of T<sub>1</sub> PNA

Upon photoexcitation to S<sub>1</sub>, PNA changes the structure from neutral form **1** to zwitterionic form **2** (see Figure IV-1) as a result of CT from the electron donating NH<sub>2</sub> group to the electron withdrawing NO<sub>2</sub> group [87,108-112]. It would be natural to expect a similar CT

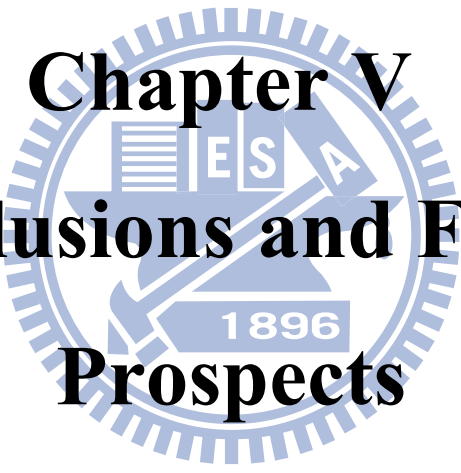
structure for  $T_1$  PNA. However, our TRIR spectroscopic results are not consistent with this hypothesis. The  $\text{NO}_2$  antisymmetric stretch shows a down shift from  $1503\text{ cm}^{-1}$  in the  $S_0$  state to  $1250\text{ cm}^{-1}$  in the  $T_1$  state, whereas the  $\text{NO}_2$  symmetric stretch and the vibrations associated with the  $\text{NH}_2$  group does not show any appreciable shift. The  $\text{NO}_2$  symmetric stretch does not show an appreciable change probably because of strong coupling with the other modes. These observations reveal that in the  $T_1$  state, charge redistribution is localized at the  $\text{NO}_2$  moiety. It is relatively easy to provide a molecular orbital picture of the  $T_1$  state. Four  $\pi$ -electrons of the  $\text{NO}_2$  moiety display the  $\pi^2\pi^{\circ 2}\pi^{*0}$  configuration in the  $S_0$  state, which is changed to  $\pi^2\pi^{\circ 1}\pi^{*1}$  in the  $T_1$  state. This change would reduce the N–O bond order from approximately 1.5 in  $S_0$  to 1.25 in  $T_1$ , which can be manifested as changes in frequency and bond length in going from  $S_0$  to  $T_1$ . The typical frequency of the  $\text{NO}_2$  antisymmetric stretch of bond order 1.5 is  $1550\text{ cm}^{-1}$  and that of the single N–O bond stretch in oximes is about  $940\text{ cm}^{-1}$ . In the present calculations, the frequency of the  $\text{NO}_2$  antisymmetric stretch mode is reduced from  $1500\text{ cm}^{-1}$  in the  $S_0$  state to  $1268\text{ cm}^{-1}$  in the  $T_1$  state. The typical length of the  $\text{N}=\text{O}$  bond is approximately  $1.2\text{ \AA}$ , whereas a single bond is  $1.4\text{ \AA}$ . As shown in Figure IV–10, the calculations reveal that the length of the  $\text{N}=\text{O}$  bond is  $1.230\text{ \AA}$  in the  $S_0$  state and  $1.271\text{ \AA}$  in the  $T_1$  state. Both observations support that the  $T_1$  state of PNA has a localized CT character. The localized CT mechanism described here is further confirmed by the shortening of the C– $\text{NO}_2$  bond upon the excitation, which is associated with the contribution of the single  $\pi^*$ -electron localized on the nitrogen atom to the aromatic ring. Such a contribution leads to a partial quinoid structure of PNA in the  $T_1$  state. Note that the picture obtained here is quite different from that given by conventional hybrids of resonance structures such as **1** and **2** in organic chemistry [87,115]. The quinoid structure is actually restricted only to the part of the phenyl ring in the vicinity of the  $\text{NO}_2$  moiety, because the C– $\text{NH}_2$  bond length is practically identical between  $S_0$  and  $T_1$  ( $1.353$  vs.  $1.352\text{ \AA}$ ; see Figure IV–10). If we are compelled to translate this partial quinoid structure into the language of resonance structures, we may find that **3** would be the closest. It is also consistent with the experimental evidence that the  $T_1$  state shows a less pronounced CT character compared with the  $S_1$  state [111].



**Figure IV-10.** Bond lengths and bond angles in the S<sub>0</sub> state (upper value) and T<sub>1</sub> state (lower value in green) derived from the DFT calculations with the PNA+2ACN model.

## IV-5 Summary

In the present study, we performed nanosecond TRIR spectroscopy of PNA and its isotopomers (PNA-<sup>15</sup>NH<sub>2</sub> and PNA-<sup>15</sup>NO<sub>2</sub>) in CD<sub>3</sub>CN and assigned the observed transient absorption bands to T<sub>1</sub> PNA. The lifetime of the T<sub>1</sub> state has been determined to be 430 ns with argon bubbling, which decreases to about one-third with oxygen bubbling. To interpret the IR spectrum of T<sub>1</sub> PNA and extract structural information on the T<sub>1</sub> state, we have simulated the IR spectra of PNA, PNA-<sup>15</sup>NH<sub>2</sub>, and PNA-<sup>15</sup>NO<sub>2</sub> in both S<sub>0</sub> and T<sub>1</sub> states at the DFT/B3LYP computational level. We have compared three different molecular models, namely, the free gas-phase molecule, the PCM model, and the explicitly solvated model, among which the explicitly solvated model with two CD<sub>3</sub>CN molecules attached to the NH<sub>2</sub> group (the PNA+2ACN model) has been found to give best agreement with experiment except for the doublet at around 1320 cm<sup>-1</sup>. This discrepancy has been completely removed by elongating the C-NH<sub>2</sub> bond slightly (0.012 Å) from its equilibrium length, and the resulting ground-state IR spectra are in excellent agreement with the experimentally recorded spectra of PNA and its isotopomers in the whole spectral region studied. The IR spectra of the three PNA isotopomers using the PNA+2ACN model with slight elongation of the C-NH<sub>2</sub> bond satisfactorily reproduced the experimental data. These results indicate that the T<sub>1</sub> PNA has a partial quinoid structure, for which the conventional way of describing excited states of push-pull molecules (i.e., the two-state models) breaks down.

The logo of the University of East Africa is a circular emblem with a gear-like border. Inside the circle, there is a shield with a book, a quill, and a scale. The letters 'E', 'S', and 'A' are arranged in a grid within the shield. Below the shield is a banner with the year '1896'.

**Chapter V**  
**Conclusions and Future**  
**Prospects**

In this Thesis, we have demonstrated that TRIR studies can advance our understanding of the structure and reactivity of transient species that play prominent roles in the functioning of OPVs. We have addressed the issue of charge recombination losses in solar cells by studying the BET reaction dynamics in the model system of Py and DCB. All the transient species involved in the BET ( $\text{Py}_2^{*+}$ ,  $\text{DCB}^{\bullet-}$ , and  $\text{ACN}_2^-$ ) have been well characterized and a simple reaction scheme has been proposed that accounts for the observed BET dynamics. We have found that ACN plays a dual role as solvent and a reactant that mediates BET from  $\text{DCB}^{\bullet-}$  to  $\text{Py}_2^{*+}$ . The BET reaction scheme shown here can have significant implications because ACN is commonly used solvent for redox couple in DSSC. Moreover, Baheti and co-workers [116] recently used Py-based dye molecules in DSSC and Maggio and co-workers [46] theoretically demonstrated the importance of orbital symmetry in minimizing the charge recombination in DSSCs. The TRIR study can be extended to more realistic systems of solar cell devices.

We have also elucidated the  $T_1$  state of PNA. It has been well characterized using TRIR spectroscopy combined with DFT/B3LYP calculations with the explicit solvation model. The  $T_1$  state of PNA has been shown to exhibit a partial quinoid structure in contrast to the zwitterionic CT structure in the two-state model. This result challenges our understanding of excited states and thus it is necessary to characterize the excited state of several other molecules of this type using TRIR and explicit solvation model.

The present comprehensive TRIR study will provide us with molecular-level understanding of condensed-phase PET reactions and may even change our perceptions about excited-state structure and reactivity. We believe that further investigation along this line will pave a new way to develop efficient materials in the future.

# References

- [1] N. J. Turro, V. Ramamurthy, and J. C. Scaiano, Modern Molecular Photochemistry of Organic Molecules, University Science Books, California, 2010.
- [2] N. Nelson and A. Ben-Shem, “The Complex Architecture of Oxygenic Photosynthesis,” *Nature Reviews Molecular Cellular Biology*, vol. 5, no. 12, pp. 971–982, Dec. 2004.
- [3] J. Barber and P. D. Tran, “From Natural to Artificial Photosynthesis,” *Journal of the Royal Society Interface*, vol. 10, p. 20120984, Jan. 2013.
- [4] M. L. Applebury, P. M. Rentzepis, and K. Peters, “Primary Photochemical Event in Vision: Proton Translocation,” *Proceedings of the National Academy of Sciences of the United States of America*, vol. 74, no. 8, p. 3119, Aug. 1977.
- [5] A. Cooper, “Energy Uptake in the First Step of Visual Excitation,” *Nature*, vol. 282, no. 5738, pp. 531–533, Nov. 1979.
- [6] R. G. W. Norrish and C. H. Bamford, “Photo-Decomposition of Aldehydes and Ketones,” *Nature*, vol. 140, no. 3535, pp. 195–196, Jul. 1937.
- [7] R. Norrish, “On the Principle of Primary Recombination in Relation to the Velocity of Thermal Reactions in Solution,” *Transactions of the Faraday Society*, vol. 33, pp. 1521–1528, 1937.
- [8] R. Exelby and R. Grinter, “Phototropy (or Photochromism),” *Chemical Reviews*, vol. 65, no. 2, pp. 247–260, Apr. 1965.
- [9] R. Pardo, M. Zayat, and D. Levy, “Photochromic Organic–Inorganic Hybrid Materials,” *Chemical Society Reviews*, vol. 40, no. 2, pp. 672–687, 2011.
- [10] N. J. Turro, “Fun with Photons, Reactive Intermediates, and Friends. Skating on the Edge of the Paradigms of Physical Organic Chemistry, Organic Supramolecular Photochemistry, and Spin Chemistry,” *Journal of Organic Chemistry*, vol. 76, no. 24, pp. 9863–9890, Dec. 2011.
- [11] D. P. DeCosta, A. K. Bennett, and J. A. Pincock, “The Norrish Type II Photofragmentation of Esters Induced by Intramolecular Electron Transfer,” *Journal of the American Chemical Society*, vol. 121, no. 15, pp. 3785–3786, Apr. 1999.
- [12] S. Yabumoto, S. Shigeto, Y. P. Lee, and H. Hamaguchi, “Ordering, Interaction, and Reactivity of the Low-Lying  $n\pi^*$  and  $\pi\pi^*$  Excited Triplet States of Acetophenone Derivatives,” *Angewandte Chemie International Edition*, vol. 49, no. 48, pp. 9201–9205, Oct. 2010.
- [13] G. Fleming, Chemical Applications of Ultrafast Spectroscopy, Oxford University Press, New York, Jan. 1986.
- [14] M. D. A. Fayer, Ultrafast Infrared And Raman Spectroscopy, CRC Press, 2001.
- [15] R. G. W. Norrish and G. Porter, “Chemical Reactions Produced by Very High Light Intensities,” *Nature*, vol. 164, no. 4172, pp. 658–658, Oct. 1949.
- [16] G. Porter, “Flash Photolysis and Spectroscopy. A New Method for the Study of Free Radical Reactions,” *Proceedings of the Royal Society A: Mathematical, Physical and Engineering Sciences*, vol. 200, no. 1061, pp. 284–300, Jan. 1950.
- [17] R. M. Bowman, M. Dantus, and A. H. Zewail, “Femtosecond Transition-State Spectroscopy of Iodine: From Strongly Bound to Repulsive Surface Dynamics,” *Chemical Physics Letters*, vol. 161, no. 4, pp. 297–302, Sep. 1989.
- [18] P. Hannaford, Femtosecond Laser Spectroscopy, Springer, 2004.
- [19] R. Berera, R. Grondelle, and J. T. M. Kennis, “Ultrafast Transient Absorption

- Spectroscopy: Principles and Application to Photosynthetic Systems,” *Photosynthesis Research*, vol. 101, no. 2, pp. 105–118, Jul. 2009.
- [20] M. Wojdyla, S. A. Gallagher, M. P. Moloney, Y. K. Gunko, J. M. Kelly, L. M. Magno, S. J. Quinn, I. P. Clark, G. M. Greetham, and M. Towrie, “Picosecond to Millisecond Transient Absorption Spectroscopy of Broad-Band Emitting Chiral CdSe Quantum Dots,” *The Journal of the Physical Chemistry C*, vol. 116, no. 30, pp. 16226–16232, Aug. 2012.
- [21] P. M. Keane, M. Wojdyla, G. W. Doorley, G. W. Watson, I. P. Clark, G. M. Greetham, A. W. Parker, M. Towrie, J. M. Kelly, and S. J. Quinn, “A Comparative Picosecond Transient Infrared Study of 1-Methylcytosine and 5'-dCMP That Sheds Further Light on the Excited States of Cytosine Derivatives,” *Journal of the American Chemical Society*, vol. 133, no. 12, pp. 4212–4215, Mar. 2011.
- [22] G. W. Doorley, M. Wojdyla, G. W. Watson, M. Towrie, A. W. Parker, J. M. Kelly, and S. J. Quinn, “Tracking DNA Excited States by Picosecond-Time-Resolved Infrared Spectroscopy: Signature Band for a Charge-Transfer Excited State in Stacked Adenine–Thymine Systems,” *The Journal of Physical Chemistry Letters*, vol. 4, no. 16, pp. 2739–2744, Aug. 2013.
- [23] S. Yabumoto, S. Sato, and H. Hamaguchi, “Vibrational and Electronic Infrared Absorption Spectra of Benzophenone in the Lowest Excited Triplet State,” *Chemical Physics Letters*, vol. 416, no. 1, pp. 100–103, Nov. 2005.
- [24] S. Tanaka, C. Kato, K. Horie, and H. Hamaguchi, “Time-Resolved Infrared Spectra and Structures of the Excited Singlet and Triplet States of Fluorenone,” *Chemical Physics Letters*, vol. 381, no. 3, pp. 385–391, Nov. 2003.
- [25] K. Iwata and H. Hamaguchi, “Microscopic Mechanism of Solute–Solvent Energy Dissipation Probed by Picosecond Time-Resolved Raman Spectroscopy,” *The Journal of Physical Chemistry A*, vol. 101, no. 4, pp. 632–637, Jan. 1997.
- [26] H. Hamaguchi, “Picosecond Solvation Dynamics of S<sub>1</sub> Trans-Stilbene by Nanosecond Transient Raman Spectroscopy with “Optical Depletion Timing”,” *The Journal of Chemical Physics*, vol. 89, no. 4, pp. 2587–2588, 1988.
- [27] M. Towrie, P. Matousek, A. W. Parker, W. T. Toner, and R. E. Hester, “The Picosecond Transient Raman Spectra of S<sub>1</sub> Excited Oligophenyls, Oxazols and Stilbene Derivatives,” *Spectrochimica Acta Part A: Molecular and Biomolecular Spectroscopy*, vol. 51, no. 14, pp. 2491–2500, Dec. 1995.
- [28] T. L. Gustafson, D. M. Roberts, and D. A. Chernoff, “Picosecond Transient Raman Spectroscopy: The Photoisomerization of Trans-Stilbene,” *The Journal of Chemical Physics*, vol. 79, no. 4, pp. 1559–1564, 1983.
- [29] S. Srivastava, E. Yourd, and J. P. Toscano, “Structural Differences between  $\pi\pi^*$  and  $n\pi^*$  Acetophenone Triplet Excited States as Revealed by Time-Resolved IR Spectroscopy,” *Journal of the American Chemical Society*, vol. 120, no. 24, pp. 6173–6174, Aug. 1998.
- [30] M. V. Encinas and J. C. Scaiano, “Reaction of Benzophenone Triplets with Allylic Hydrogens. Laser Flash Photolysis Study,” *Journal of the American Chemical Society*, vol. 103, no. 21, pp. 6393–6397, Oct. 1981.
- [31] V. Balzani, P. Piotrowiak, M. A. J. Rodgers, J. Mattay, D. Astruc, H. B. Gray, J. Winkler, S. Fukuzumi, T. E. Mallouk, Y. Haas, A. P. de Silva, and I. Gould, *Electron Transfer in Chemistry, Principles, Theories, Methods, and Techniques*, vol. 1. Wiley-VCH, 2001.
- [32] T. Yuzawa, C. Kato, M. W. George, and H. Hamaguchi, “Nanosecond Time-Resolved Infrared Spectroscopy with a Dispersive Scanning Spectrometer,” *Applied Spectroscopy*, vol. 48, no. 6, pp. 684–690, Jun. 1994.

- [33] S. Yabumoto, "Development of Highly-Sensitive and High-Speed Nanosecond Time-Resolved Mid-/Near-infrared Spectrometer and Its Application to Photochemistry of Aromatic Carbonyl Compounds," The University of Tokyo, PhD Thesis, Dec. 2007.
- [34] Y. Sasaki and H. Hamaguchi, "Time-resolved Raman Study on the Photoinduced Intermolecular Electron-Transfer Reaction of Biphenyl in Alcohols," *The Journal of Chemical Physics*, vol. 110, no. 18, pp. 9179–9185, 1999.
- [35] V. Kozich, W. Werncke, J. Dreyer, K. W. Brzezinka, M. Rini, A. Kummrow, and T. Elsaesser, "Vibrational Excitation and Energy Redistribution after Ultrafast Internal Conversion in 4-Nitroaniline," *The Journal of Chemical Physics*, vol. 117, no. 2, pp. 719–726, 2002.
- [36] P. Chen and R. A. Palmer, "Ten-Nanosecond Step-Scan FT-IR Absorption Difference Time-Resolved Spectroscopy: Applications to Excited States of Transition Metal Complexes," *Applied Spectroscopy*, vol. 51, no. 4, pp. 580–583, Apr. 1997.
- [37] T. Yuzawa and H. Hamaguchi, "Triplet Quantum Chain Process in the Photoisomerization of 9-cis Retinal as Revealed by Nanosecond Time-Resolved Infrared Spectroscopy," *Journal of Molecular Structure*, vol. 976, no. 1, pp. 414–418, Jul. 2010.
- [38] T. Yuzawa and H. Hamaguchi, "Investigation of the Photoisomerization of all-Trans-Retinal by Singular-Value-Decomposition Analysis of Nanosecond Time-Resolved Infrared Spectra," *Journal of Molecular Structure*, vol. 352, pp. 489–495, Jun. 1995.
- [39] J. Sasaki, T. Yuzawa, H. Kandori, A. Maeda, and H. Hamaguchi, "Nanosecond Time-Resolved Infrared Spectroscopy Distinguishes two K species in the Bacteriorhodopsin Photocycle," *Biophysical Journal*, vol. 68, no. 5, pp. 2073–2080, May 1995.
- [40] G. Puxty, M. Maeder, and K. Hungerbühler, "Tutorial on the Fitting of Kinetics Models to Multivariate Spectroscopic Measurements with Non-Linear Least-Squares Regression," *Chemometrics and Intelligent Laboratory Systems*, vol. 81, no. 2, pp. 149–164, 2006.
- [41] N. Mataga, T. Okada, and H. Masuhara, Eds., Dynamics and Mechanisms of Photoinduced Electron Transfer and Related Phenomena, Elsevier, Amsterdam, 1992.
- [42] G. J. Kavarnos, Fundamentals of Photoinduced Electron Transfer, John Wiley & Sons, Australia, 1993.
- [43] S. Handa, H. Wietasch, M. Thelakkat, J. R. Durrant, and S. A. Haque, "Reducing Charge Recombination Losses in Solid State Dye Sensitized Solar Cells: the use of Donor-Acceptor Sensitizer Dyes.," *Chemical Communications*, no. 17, pp. 1725–1727, May 2007.
- [44] A. Hagfeldt, G. Boschloo, L. Sun, L. Kloo, and H. Pettersson, "Dye-Sensitized Solar Cells," *Chemical Reviews*, vol. 110, no. 11, pp. 6595–6663, Nov. 2010.
- [45] S. R. Cowan, N. Banerji, W. L. Leong, and A. J. Heeger, "Charge Formation, Recombination and Sweep-Out Dynamics in Organic Solar Cells," *Advanced Functional Materials*, vol. 22, no. 6, pp. 1116–1128, Jan. 2012.
- [46] E. Maggio, G. C. Solomon, and A. Troisi, "Exploiting Quantum Interference in Dye Sensitized Solar Cells," *ACS Nano*, vol. 8, no. 1, pp. 409–418, Jan. 2014.
- [47] Y. Tachibana, J.-E. Moser, M. Grätzel, D. R. Klug, and J. R. Durrant, "Subpicosecond Interfacial Charge Separation in Dye-Sensitized Nanocrystalline Titanium Dioxide Films," *The Journal of Physical Chemistry*, vol. 100, no. 51, pp.



- 20056–20062, 1996.
- [48] J. B. Asbury, R. J. Ellingson, H. N. Ghosh, S. Ferrere, A. J. Nozik, and T. Lian, “Femtosecond IR Study of Excited-State Relaxation and Electron-Injection Dynamics of Ru(dcbpy)<sub>2</sub>(NCS)<sub>2</sub> in Solution and on Nanocrystalline TiO<sub>2</sub> and Al<sub>2</sub>O<sub>3</sub> Thin Films,” *The Journal of Physical Chemistry B*, vol. 103, no. 16, pp. 3110–3119, Apr. 1999.
- [49] M. Wielopolski, J.-H. Kim, Y.-S. Jung, Y.-J. Yu, K.-Y. Kay, T. W. Holcombe, S. M. Zakeeruddin, M. Grätzel, and J.-E. Moser, “Position-Dependent Extension of  $\pi$ -Conjugation in D- $\pi$ -A Dye Sensitizers and the Impact on the Charge-Transfer Properties,” *The Journal of Physical Chemistry C*, vol. 117, no. 27, pp. 13805–13815, 2013.
- [50] G. Grancini, D. Polli, D. Fazzi, J. Cabanillas-Gonzalez, G. Cerullo, and G. Lanzani, “Transient Absorption Imaging of P3HT:PCBM Photovoltaic Blend: Evidence For Interfacial Charge Transfer State,” *The Journal of Physical Chemistry Letters*, vol. 2, no. 9, pp. 1099–1105, May 2011.
- [51] H. Ohkita and S. Ito, “Transient Absorption Spectroscopy of Polymer-Based Thin-Film Solar Cells,” *Polymer*, vol. 52, no. 20, pp. 4397–4417, Sep. 2011.
- [52] D. A. Vithanage, A. Devižis, V. Abramavičius, Y. Infahsaeng, D. Abramavičius, R. C. I. MacKenzie, P. E. Keivanidis, A. Yartsev, D. Hertel, J. Nelson, V. Sundström, and V. Gulbinas, “Visualizing Charge Separation in Bulk Heterojunction Organic Solar cells,” *Nature Communications*, vol. 4, p. 2234, Aug. 2013.
- [53] T. Hino, H. Akazawa, H. Masuhara, and N. Mataga, “Ionic Photodissociation of Excited Electron Donor-Acceptor Systems. II. Importance of the Chemical Property of Donor-Acceptor Pairs,” *The Journal of Physical Chemistry*, vol. 80, no. 1, pp. 33–37, 1976.
- [54] T. Hino, H. Masuhara, and N. Mataga, “The Formation and Dissociation of the Solvated Ion-pair in the Excited Pyrene–Dicyanobenzene System,” *Bulletin of the Chemical Society of Japan*, vol. 49, no. 2, pp. 394–396, 1976.
- [55] M. Koch, R. Letrun, and E. Vauthey, “Exciplex Formation in Bimolecular Photoinduced Electron-Transfer Investigated by Ultrafast Time-Resolved Infrared Spectroscopy,” *Journal of the American Chemical Society*, vol. 136, no. 10, pp. 4066–4074, Mar. 2014.
- [56] O. F. Mohammed, K. Adamczyk, N. Banerji, J. Dreyer, B. Lang, E. T. J. Nibbering, and E. Vauthey, “Direct Femtosecond Observation of Tight and Loose Ion Pairs upon Photoinduced Bimolecular Electron Transfer,” *Angewandte Chemie International Edition*, vol. 47, no. 47, pp. 9044–9048, Nov. 2008.
- [57] O. F. Mohammed and E. Vauthey, “Simultaneous Generation of Different Types of Ion Pairs upon Charge-Transfer Excitation of a Donor–Acceptor Complex Revealed by Ultrafast Transient Absorption Spectroscopy,” *The Journal of Physical Chemistry A*, vol. 112, no. 26, pp. 5804–5809, Jun. 2008.
- [58] S. Narra, S.-W. Chang, H. A. Witek, and S. Shigeto, “Is Our Way of Thinking about Excited States Correct? Time-Resolved Dispersive IR Study on p-Nitroaniline,” *Chemistry European Journal*, vol. 18, no. 9, pp. 2543–2550, Jan. 2012.
- [59] K. H. Grellmann, A. R. Watkins, and A. Weller, “Electron-Transfer Mechanism of Fluorescence Quenching in Polar Solvents. I. Dicyanobenzene as Quencher,” *The Journal of Physical Chemistry*, vol. 76, no. 4, pp. 469–473, Feb. 1972.
- [60] H. Masuhara and N. Mataga, “Ionic Photodissociation of Electron Donor-Acceptor Systems in Solution,” *Accounts of Chemical Research*, vol. 14, no. 10, pp. 312–318, Oct. 1981.

- [61] Y. Hirata, Y. Kanda, and N. Mataga, "Picosecond Laser Photolysis and Transient Photocurrent Studies of the Ionic Dissociation Mechanism of Heteroexcimers: Pyrene-N,N-Dimethylaniline and Pyrene-p-Dicyanobenzene Systems in Polar Solvents," *The Journal of Physical Chemistry*, vol. 87, no. 10, pp. 1659–1662, May 1983.
- [62] M. Baba, M. Saitoh, Y. Kowaka, K. Taguma, K. Yoshida, Y. Semba, S. Kasahara, T. Yamanaka, Y. Ohshima, Y. C. Hsu, and S. H. Lin, "Vibrational and Rotational Structure and Excited-State Dynamics of Pyrene," *The Journal of Chemical Physics*, vol. 131, no. 22, p. 224318, Dec. 2009.
- [63] H. Nakashima, T. Shida, and H. Nakatsuji, "Electronic Excitation Spectra of Radical Anions of Cyanoethylenes and Cyanobenzenes: Symmetry Adapted Cluster–Configuration Interaction Study," *The Journal of Chemical Physics*, vol. 136, no. 21, p. 214306, 2012.
- [64] G. Boschloo and A. Hagfeldt, "Characteristics of the Iodide/Triiodide Redox Mediator in Dye-Sensitized Solar Cells," *Accounts of Chemical Research*, vol. 42, no. 11, pp. 1819–1826, Nov. 2009.
- [65] I. Montanari, J. Nelson, and J. R. Durrant, "Iodide Electron Transfer Kinetics in Dye-Sensitized Nanocrystalline TiO<sub>2</sub> Films," *The Journal of Physical Chemistry B*, vol. 106, no. 47, pp. 12203–12210, Nov. 2002.
- [66] S. Pelet, J.-E. Moser, and M. Grätzel, "Cooperative Effect of Adsorbed Cations and Iodide on the Interception of Back Electron Transfer in the Dye Sensitization of Nanocrystalline TiO<sub>2</sub>," *The Journal of Physical Chemistry B*, vol. 104, no. 8, pp. 1791–1795, Mar. 2000.
- [67] A. D. Becke, "Density-Functional Thermochemistry. III. The Role of Exact Exchange," *The Journal of Chemical Physics*, vol. 98, no. 7, p. 5648, 1993.
- [68] C. Lee, W. Yang, and R. G. Parr, "Development of the Colle-Salvetti Correlation-Energy Formula into a Functional of the Electron Density," *Physical Reviews B*, vol. 37, no. 2, pp. 785–789, Jan. 1988.
- [69] S. Grimme, J. Antony, S. Ehrlich, and H. Krieg, "A Consistent and Accurate Ab Initio Parametrization of Density Functional Dispersion Correction (DFT-D) for the 94 Elements H-Pu," *The Journal of Chemical Physics*, vol. 132, no. 15, p. 154104, Apr. 2010.
- [70] T. H. Dunning, "Gaussian Basis Sets for use in Correlated Molecular Calculations. I. The Atoms Boron through Neon and Hydrogen," *The Journal of Chemical Physics*, vol. 90, no. 2, p. 1007, 1989.
- [71] R. A. Kendall, T. H. Dunning, and R. J. Harrison, "Electron Affinities of the First-Row Atoms Revisited. Systematic Basis Sets and Wave Functions," *The Journal of Chemical Physics*, vol. 96, no. 9, pp. 6796–6806, 1992.
- [72] G. E. Scuseria, M. A. Robb, J. R. Cheeseman, G. Scalmani, V. Barone, B. Mennucci, G. A. Petersson, H. Nakatsuji, M. Caricato, and X. Li, "*Gaussian 09, revision a. 02*," Gaussian Inc., Wallingford Ct, 2009.
- [73] M. Hara, S. Tojo, K. Kawai, and T. Majima, "Formation and Decay of Pyrene Radical Cation and Pyrene Dimer Radical Cation in the Absence and Presence of Cyclodextrins during Resonant Two-Photon Ionization of Pyrene and Sodium 1-pyrene sulfonate," *Physical Chemistry Chemical Physics*, vol. 6, no. 13, pp. 3215–3220, Jul. 2004.
- [74] S. Samori, M. Fujitsuka, and T. Majima, "Photodissociation of Pyrene Dimer Radical Cation during the Pulse Radiolysis–Laser Flash Photolysis Combined Method," *Research on Chemical Intermediates*, vol. 39, no. 1, pp. 449–461, Jan. 2013.

- [75] A. Kira, S. Arai, and M. Imamura, "Pyrene Dimer Cation as Studied by Pulse Radiolysis," *The Journal of Chemical Physics*, vol. 54, no. 11, p. 4890, 1971.
- [76] M. A. J. Rodgers, "Formation Kinetics of the Pyrene Dimer Cation Observed by Pulse Radiolysis," *Chemical Physics Letters*, vol. 9, no. 2, pp. 107–108, Apr. 1971.
- [77] J. K. Kochi, R. Rathore, and P. L. Maguères, "Stable Dimeric Aromatic Cation–Radicals. Structural and Spectral Characterization of Through-Space Charge Delocalization," *Journal of Organic Chemistry*, vol. 65, no. 21, pp. 6826–6836, Oct. 2000.
- [78] B. Badger and B. Brocklehurst, "Absorption Spectra of Dimer Cations. Part 2. Benzene derivatives," *Transactions of the Faraday Society*, vol. 65, no. 0, pp. 2582–2587, 1969.
- [79] M. W. Geiger and N. J. Turro, "Pyrene Fluorescence Lifetime as a Probe for Oxygen Penetration of Micelles," *Photochemistry Photobiology*, vol. 22, no. 6, pp. 273–276, Dec. 1975.
- [80] J. R. Lakowicz and G. Weber, "Quenching of Fluorescence by Oxygen. Probe for Structural Fluctuations in Macromolecules," *Biochemistry*, vol. 12, no. 21, pp. 4161–4170, 1973.
- [81] I. A. Shkrob and M. C. Sauer, "Electron Localization in Liquid Acetonitrile," *The Journal of Physical Chemistry A*, vol. 106, no. 39, pp. 9120–9131, 2002.
- [82] C. Xia, J. Peon, and B. Kohler, "Femtosecond Electron Ejection in Liquid Acetonitrile: Evidence for Cavity Electrons and Solvent Anions," *The Journal of Chemical Physics*, vol. 117, no. 19, pp. 8855–8866, 2002.
- [83] I. A. Shkrob, K. Takeda, and F. Williams, "Electron Localization in Solid Acetonitrile," *The Journal of Physical Chemistry A*, vol. 106, no. 39, pp. 9132–9144, 2002.
- [84] S. C. Doan and B. J. Schwartz, "Ultrafast Studies of Excess Electrons in Liquid Acetonitrile: Revisiting the Solvated Electron/Solvent Dimer Anion Equilibrium," *The Journal of Physical Chemistry B*, vol. 117, no. 16, pp. 4216–4221, Apr. 2013.
- [85] S. C. Doan and B. J. Schwartz, "Nature of Excess Electrons in Polar Fluids: Anion-Solvated Electron Equilibrium and Polarized Hole-Burning in Liquid Acetonitrile," *The Journal of Physical Chemistry Letters*, vol. 4, no. 9, pp. 1471–1476, May 2013.
- [86] T. Takayanagi, T. Hoshino, and K. Takahashi, "Electronic Structure Calculations of Acetonitrile Cluster Anions: Stabilization Mechanism of Molecular Radical Anions by Solvation," *Chemical Physics*, vol. 324, no. 2, pp. 679–688, 2006.
- [87] A. M. Moran and A. M. Kelley, "Solvent Effects on Ground and Excited Electronic State Structures of p-Nitroaniline," *The Journal of Chemical Physics*, vol. 115, no. 2, p. 912, 2001.
- [88] S. P. Karna, P. N. Prasad, and M. Dupuis, "Nonlinear Optical Properties of p-Nitroaniline: An Ab Initio Time-Dependent Coupled Perturbed Hartree–Fock Study," *The Journal of Chemical Physics*, vol. 94, no. 2, pp. 1171–1181, 1991.
- [89] C. Castiglioni, M. Del Zoppo, and G. Zerbi, "Molecular First Hyperpolarizability of Push-Pull Polyenes: Relationship between Electronic and Vibrational Contribution by a Two-State Model," *Physical Reviews B*, vol. 53, no. 20, pp. 13319–13325, May 1996.
- [90] C. Dehu, F. Meyers, E. Hendrickx, K. Clays, A. Persoons, S. R. Marder, and J. L. Bredas, "Solvent Effects on the Second-Order Nonlinear Optical Response of  $\pi$ -Conjugated Molecules: A Combined Evaluation through Self-Consistent Reaction Field Calculations and Hyper-Rayleigh Scattering Measurements," *Journal of the American Chemical Society*, vol. 117, no. 40, pp. 10127–10128, Oct. 1995.
- [91] J. N. Woodford, M. A. Pauley, and C. H. Wang, "Solvent Dependence of the First

- Molecular Hyperpolarizability of p-Nitroaniline Revisited,” *The Journal of Physical Chemistry A*, vol. 101, no. 11, pp. 1989–1992, 1997.
- [92] F. L. Huyskens, P. L. Huyskens, and A. P. Persoons, “Solvent Dependence of the First Hyperpolarizability of p-Nitroanilines: Differences between Nonspecific Dipole–Dipole Interactions and Solute–Solvent H-bonds,” *The Journal of Chemical Physics*, vol. 108, no. 19, pp. 8161–8171, 1998.
- [93] P. E. Larsson, L. M. Kristensen, and K. V. Mikkelsen, “Studies of Hyperpolarizabilities for para-Nitroaniline in the Charge-Transfer State: Application of a Reaction-F Response Method,” *International journal of quantum chemistry*, vol. 75, no. 4, pp. 449–456, 1999.
- [94] F. Sim, S. Chin, M. Dupuis, and J. E. Rice, “Electron Correlation Effects in Hyperpolarizabilities of p-Nitroaniline,” *The Journal of Physical Chemistry*, vol. 97, no. 6, pp. 1158–1163, Feb. 1993.
- [95] T. P. Carsey, G. L. Findley, and S. P. McGlynn, “Systematics in the Electronic Spectra of Polar Molecules. 1. Para-disubstituted Benzenes,” *Journal of the American Chemical Society*, vol. 101, no. 16, pp. 4502–4510, 1979.
- [96] J. Dreyer, V. Kozich, and W. Werncke, “Tuning Intramolecular Anharmonic Vibrational Coupling in 4-Nitroaniline by Solvent-Solute Interaction,” *The Journal of Chemical Physics*, vol. 127, no. 23, p. 234505, Dec. 2007.
- [97] K. Mohanalingam, D. Yokoyama, C. Kato, and H. Hamaguchi, “Three Distinct Solvated Structures of p-Nitroaniline in Acetonitrile/CCl<sub>4</sub> Mixed Solvents: A Combined Singular Value Decomposition Analysis of Ultraviolet Absorption and Raman Spectra,” *Bulletin of the Chemical Society of Japan*, vol. 72, no. 3, pp. 389–395, 1999.
- [98] T. Fujisawa, M. Terazima, and Y. Kimura, “Solvent Effects on the Local Structure of p-Nitroaniline in Supercritical Water and Supercritical Alcohols,” *The Journal of Physical Chemistry A*, vol. 112, no. 24, pp. 5515–5526, Jun. 2008.
- [99] T. Gunaratne, J. R. Challa, and M. C. Simpson, “Energy Flow in Push–Pull Chromophores: Vibrational Dynamics in para-Nitroaniline,” *Chemphyschem*, vol. 6, no. 6, pp. 1157–1163, 2005.
- [100] K. Kumar and P. R. Carey, “Resonance Raman Spectra and Structure of some Complex Nitroaromatic Molecules,” *The Journal of Chemical Physics*, vol. 63, no. 9, p. 3697, 1975.
- [101] E. D. Schmid, M. Moschallski, and W. L. Peticolas, “Solvent Effects on the Absorption and Raman spectra of Aromatic Nitro Compounds. Part 1. Calculation of Preresonance Raman Intensities,” *The Journal of Physical Chemistry*, vol. 90, no. 11, pp. 2340–2346, May 1986.
- [102] S. Shigeto, H. Hiramatsu, and H. Hamaguchi, “Structure and Dipole Moments of the Two Distinct Solvated Forms of p-Nitroaniline in Acetonitrile/CCl<sub>4</sub> as Studied by Infrared Electroabsorption Spectroscopy,” *The Journal of Physical Chemistry A*, vol. 110, no. 10, pp. 3738–3743, Mar. 2006.
- [103] H. Ma, S. Yao, J. Zhang, C. Pu, S. Zhao, M. Wang, and J. Xiong, “Steady-State and Transient Photolysis of p-Nitroaniline in Acetonitrile,” *Journal of Photochemistry and Photobiology A*, vol. 202, no. 1, pp. 67–73, Feb. 2009.
- [104] V. Chiş, M. M. Venter, N. Leopold, and O. Cozar, “Raman, Surface-Enhanced Raman Scattering and DFT Study of para-Nitroaniline,” *Vibrational Spectroscopy*, vol. 48, no. 2, pp. 210–214, Nov. 2008.
- [105] E. Kavitha, N. Sundaraganesan, and S. Sebastian, “Molecular structure, Vibrational Spectroscopic and HOMO-LUMO studies of 4-Nitroaniline by Density Functional Method,” *Indian Journal of Pure and Applied Physics*, vol. 48, pp. 20–30, 2010.

- [106] D. Kosenkov and L. V. Slipchenko, "Solvent Effects on the Electronic Transitions of p-Nitroaniline: A QM/EFP Study," *The Journal of Physical Chemistry A*, vol. 115, no. 4, pp. 392–401, Feb. 2011.
- [107] G. Scalmani, M. J. Frisch, B. Mennucci, J. Tomasi, R. Cammi, and V. Barone, "Geometries and Properties of Excited States in the Gas Phase and in Solution: Theory and Application of a Time-Dependent Density Functional Theory Polarizable Continuum Model," *The Journal of Chemical Physics*, vol. 124, no. 9, p. 094107, Mar. 2006.
- [108] H. K. Sinha and K. Yates, "On the Ground and Excited State Dipole Moments of Planar vs. Twisted Nitroaniline Analogues," *Canadian Journal of Chemistry*, vol. 69, no. 3, pp. 550–557, Mar. 1991.
- [109] V. M. Farztdinov, R. Schanz, S. A. Kovalenko, and N. P. Ernsting, "Relaxation of Optically Excited p-Nitroaniline: Semiempirical Quantum-Chemical Calculations Compared to Femtosecond Experimental Results," *The Journal of Physical Chemistry A*, vol. 104, no. 49, pp. 11486–11496, Dec. 2000.
- [110] S. A. Kovalenko, R. Schanz, V. M. Farztdinov, H. Hennig, and N. P. Ernsting, "Femtosecond Relaxation of Photoexcited para-Nitroaniline: Solvation, Charge transfer, Internal Conversion and Cooling," *Chemical Physics Letters*, vol. 323, no. 3, pp. 312–322, Jun. 2000.
- [111] W. Schuddeboom, J. M. Warman, H. A. M. Biemans, and E. W. Meijer, "Dipolar Triplet States of p-Nitroaniline and N-Alkyl Derivatives with One-, Two-, and Three-Fold Symmetry," *The Journal of Physical Chemistry*, vol. 100, no. 30, pp. 12369–12373, Jan. 1996.
- [112] C. L. Thomsen, J. Thøgersen, and S. R. Keiding, "Ultrafast Charge-Transfer Dynamics: Studies of p-Nitroaniline in Water and Dioxane," *The Journal of Physical Chemistry A*, vol. 102, no. 7, pp. 1062–1067, Feb. 1998.
- [113] J. Wolleben and A. C. Testa, "Charge Transfer Triplet State of p-Nitroaniline," *The Journal of Physical Chemistry*, vol. 81, no. 5, pp. 429–431, 1977.
- [114] W.-G. Chen and M. S. Braiman, "Kinetic Analysis of Time-Resolved Infrared Difference Spectra Of The L and M Intermediates of Bacterorhodopsin ," *Photochemistry Photobiology*, vol. 54, no. 6, pp. 905–910, Dec. 1991.
- [115] P. C. Hiberty and G. Ohanessian, "Valence-Bond Description of Conjugated Molecules. 3. The Through-Resonance Concept in para-Substituted Nitrobenzenes," *Journal of the American Chemical Society*, vol. 106, no. 23, pp. 6963–6968, Nov. 1984.
- [116] A. Baheti, C.-P. Lee, K. R. J. Thomas, and K.-C. Ho, "Pyrene-based Organic Dyes with Thiophene containing  $\pi$ -linkers for Dye-Sensitized Solar Cells: Optical, Electrochemical and Theoretical Investigations," *Physical Chemistry Chemical Physics*, vol. 13, no. 38, pp. 17210–17221, 2011.